Cell Reports
Medicine

Article

Integrative CSF profiling identifies disease-specific immune responses in leptomeningeal disease

Graphical abstract

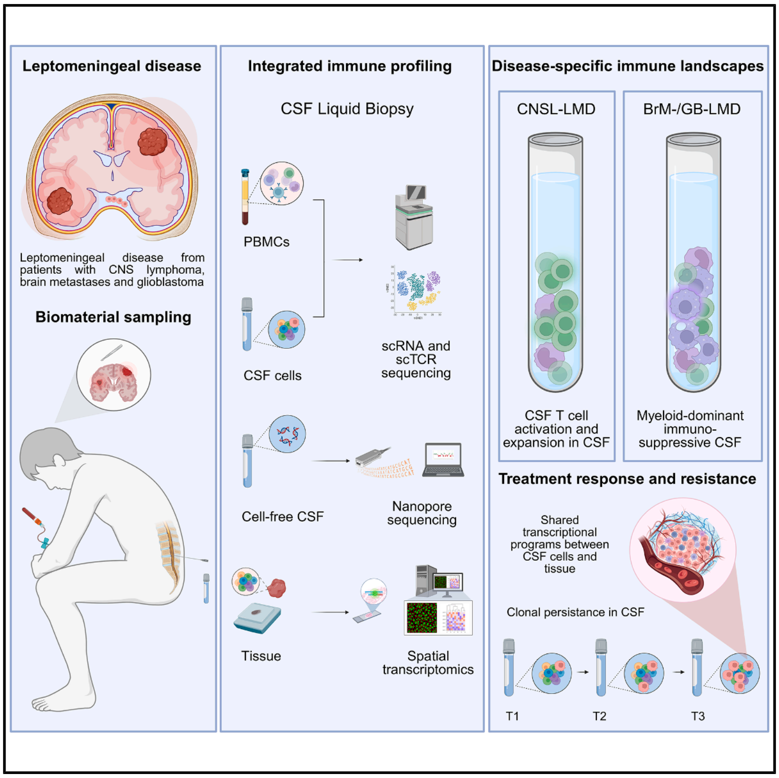

Highlights

- Single-cell CSF profiling reveals disease-specific immune landscapes in LMD
- CNSL-LMD shows pronounced T cell activation and clonal T cell expansion in the CSF
- LMD from BrMs and GB exhibits myeloid-dominant CSF profiles
- Longitudinal CSF analysis tracks treatment response and tumor progression

Authors

Paula Nieto, Svenja Klinsing,
Ginevra Caratù, ..., Holger Heyn,
Pia S. Zeiner, Juan C. Nieto

Correspondence

juan.nieto@cnag.eu (J.C.N.),
holger.heyn@cnag.eu (H.H.),
zeiner@med.uni-frankfurt.de (P.S.Z.)

In brief

Nieto et al. profile cerebrospinal fluid cells in leptomeningeal disease across tumor entities and compare them with blood and tissue lesions using single-cell and spatial approaches, showing that the CSF is an immune-active compartment reflecting immune responses holding the potential to capture treatment resistance and tumor progression.

Nieto et al., 2026, Cell Reports Medicine 7, 102651
March 17, 2026
https://doi.org/10.1016/j.xcrm.2026.102651

CellPress

Please cite this article in press as: Nieto et al., Integrative CSF profiling identifies disease-specific immune responses in leptomeningeal disease, Cell Reports Medicine (2026), https://doi.org/10.1016/j.xcrm.2026.102651

Cell Reports Medicine

CellPress
OPEN ACCESS

Article

Integrative CSF profiling identifies disease-specific immune responses in leptomeningeal disease

Paula Nieto,[1,2] Svenja Klinsing,[3,4,5] Ginevra Caratù,[1] Mareike Dettki,[3] Domenica Marchese,[1] Katharina J. Weber,[5,6,7,8] Samuel Morabito,[1] Patricia Lorden,[1] Irene Ruano,[1] Katharina Imkeller,[5,6,7,8] M. Angels Velasco,[9] Silvia Vidal,[9] Juan L. Melero,[10] Philipp Euskirchen,[11,12] Marcus Czabanka,[5,7,8,13] Karl H. Plate,[5,6,7,8] Patrick N. Harter,[14] Anna Pascual-Reguant,[1] Joachim P. Steinbach,[3,5,7,8] Holger Heyn,[1,15,16,17,*] Pia S. Zeiner,[3,4,5,7,8,17,*] and Juan C. Nieto[1,17,18,*]

[1]Centro Nacional de Análisis Genómico (CNAG), Barcelona, Spain
[2]Universitat Pompeu Fabra (UPF), Barcelona, Spain
[3]Goethe University Frankfurt, University Hospital, Dr. Senckenberg Institute of Neurooncology, Frankfurt, Germany
[4]Goethe University Frankfurt, University Hospital, Department of Neurology, Frankfurt, Germany
[5]Goethe University Frankfurt, University Hospital, University Cancer Center (UCT), Frankfurt, Germany
[6]Goethe University Frankfurt, University Hospital, Institute of Neurology (Edinger-Institute), Frankfurt, Germany
[7]Goethe University Frankfurt, Frankfurt Cancer Institute (FCI), Frankfurt, Germany
[8]German Cancer Research Center (DKFZ) Heidelberg, Germany and German Cancer Consortium (DKTK), Partner Site Frankfurt/Mainz, Frankfurt, Germany
[9]Biomedical Research Institut Sant Pau (IIB Sant Pau), Barcelona, Spain
[10]Omniscope Inc., Barcelona, Spain
[11]Charité - Universitätsmedizin Berlin, corporate member of Freie Universität Berlin und Humboldt Universität zu Berlin, Department of Neuropathology, Berlin, Germany
[12]German Cancer Consortium (DKTK), partner site Berlin, a partnership between DKFZ and Charité - Universitätsmedizin Berlin, Berlin, Germany
[13]Goethe University Frankfurt, University Hospital, Department of Neurosurgery, Frankfurt, Germany
[14]Center for Neuropathology and Prion Research, Ludwig-Maximilians-Universität München, Munich, Germany
[15]University of Barcelona (UB), Barcelona, Spain
[16]ICREA, Barcelona, Spain
[17]Senior author
[18]Lead contact
*Correspondence: juan.nieto@cnag.eu (J.C.N.), holger.heyn@cnag.eu (H.H.), zeiner@med.uni-frankfurt.de (P.S.Z.)
https://doi.org/10.1016/j.xcrm.2026.102651

SUMMARY

Leptomeningeal disease (LMD) is a devastating manifestation of advanced cancer, marked by rapid neurological decline and limited treatment options. Immune profiling in central nervous system (CNS) neoplasms, including LMD, is critical for understanding disease biology and guiding therapy. Here, we use single-cell RNA and T cell receptor (TCR) sequencing of cerebrospinal fluid (CSF) from patients with CNS lymphoma (CNSL), brain metastases (BrMs), and glioblastoma (GB), alongside deep TCR sequencing of blood and spatial transcriptomics of brain lesions. We uncover distinct, disease-specific CSF immune landscapes: CNSL-associated LMD shows clonal T cell expansion, while BrMs and GB are enriched in blood-derived and resident-like myeloid cells. Spatial analysis confirms transcriptional similarities between CSF and tumor microenvironments. Longitudinal sampling reveals dynamic immune changes and emerging resistant clones. These findings establish the CSF as an immune-active compartment reflecting disease-specific features and highlight the value of CSF liquid biopsy for immune monitoring and therapeutic stratification in LMD.

INTRODUCTION

Despite an inherently reduced immune response capacity of the central nervous system (CNS),[1,2] immune cells ensure surveillance and anti-tumor immune response also in the tumor microenvironment (TME) of CNS tumors.[3,4] This opens therapeutic avenues for patients with brain and leptomeningeal neoplasms,[5,6] for whom conventional treatments, including immunotherapies, have yielded limited success.[7,8] This is particularly relevant for leptomeningeal disease (LMD) arising from brain metastases (BrMs), most commonly breast cancer, lung cancer, and melanoma,[9] as well as rarer forms such as glioblastoma (GB). Although effective in hematological malignancies, immunotherapy remains challenging in CNS lymphomas (CNSL),[6,10]

Please cite this article in press as: Nieto et al., Integrative CSF profiling identifies disease-specific immune responses in leptomeningeal disease, Cell Reports Medicine (2026), https://doi.org/10.1016/j.xcrm.2026.102651

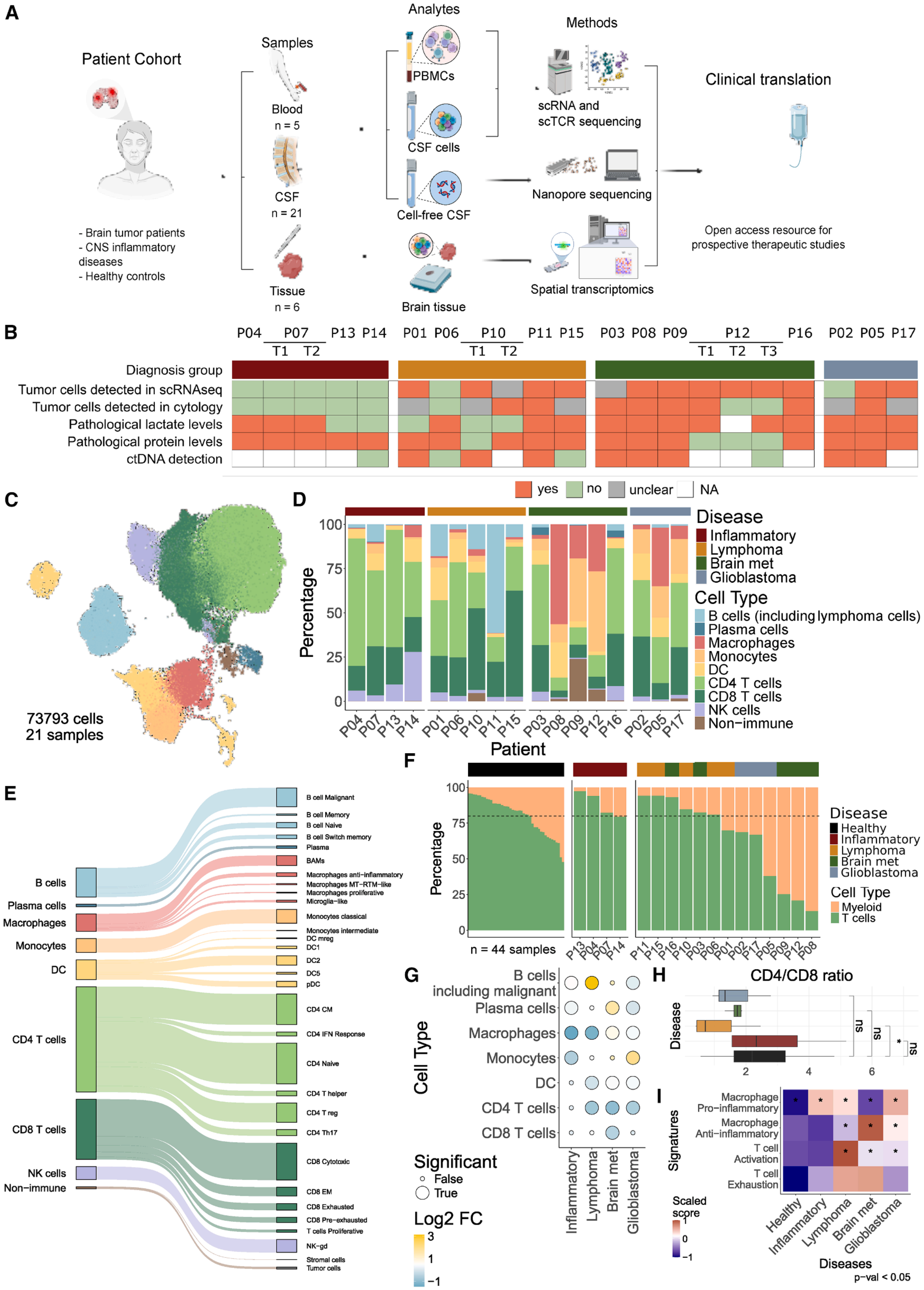

Figure 1. Single-cell phenotyping of CSF reveals complex environments driven by CNS diseases

(A) Study workflow. Schematics were created using BioRender.

(B) Square chart showing all CSF samples, several clinical parameters, as well as the detection, or lack thereof, of tumor cells by scRNA-seq.

(legend continued on next page)

Please cite this article in press as: Nieto et al., Integrative CSF profiling identifies disease-specific immune responses in leptomeningeal disease, Cell Reports Medicine (2026), https://doi.org/10.1016/j.xcrm.2026.102651

especially with concurrent LMD, due to CNS immunobiology and aggressiveness of CNSL. While multiple entry routes have been described for LMD formation, the immune landscape underlying tumor spread to the leptomeninges and cerebrospinal fluid (CSF) in LMD remain poorly understood.[6,11]

The minimally invasive liquid biopsy (LB) of CSF is particularly advantageous for the diagnosis and longitudinal monitoring of patients with LMD. Recent single-cell transcriptomic analysis of LMD has begun to uncover the immune and tumor landscape of this compartment, highlighting immunotherapy response correlation with the immune cell response within the TME.[12] Emerging CSF LB technologies hold promise for predicting prognostic outcomes.[6,13] Single-cell sequencing technologies have revolutionized our understanding of cellular diversity by providing comprehensive maps of cell types, states, and functions at unprecedented resolution.[14,15] They enable patient stratification, aiding in the identification of distinct disease types and paving the way for more precise therapeutic interventions.[16] We aim to highlight how single-cell technologies can expand CSF LB, providing valuable insights into immune responses beyond the standard cell-free CSF analytes.[6]

In contrast to healthy conditions,[10,17] the CSF changes substantially under pathological conditions, reflecting immune responses in this compartment.[9,18] For example, in patients with BrMs, identical T cell receptor (TCR) clonotypes have been identified in tumor tissue and CSF, suggesting T cell trafficking.[19] Also, CSF exhibits strong differences in the expression of interferon-induced, cytotoxic, and exhaustion genes on T cells following immunotherapy.[12] The extent to which immune responses in CNS tumors and especially in LMD are reflected in the CSF remains unclear, with single-cell technologies offering a promising means to resolve this. This study aims to create a resource that helps to decode CSF cellular landscapes in LMD across different entities using single-cell RNA and TCR sequencing, combined with the analysis of blood cells through deep TCR sequencing and matching brain tissue lesions through spatial transcriptomics.

RESULTS

Single-cell analysis of CSF reveals distinct immune dynamics

We assessed the cell landscape in the CSF applying single-cell RNA sequencing (scRNA-seq) with paired TCR sequencing in patients with LMD (CNSL, GB, and BrMs) compared to neuro-inflammatory disorders (Table S1). CSF was compared to the blood samples and corresponding CNS tissues profiled by deep immune receptor sequencing (Omniscope AI's T cell receptor sequencing technology [OS-TCR]) and spatial transcriptomics, respectively. Additionally, circulating tumor DNA (ctDNA) was assessed in corresponding cell-free CSF by Nanopore sequencing (Figures 1A and S1A). Flow cytometric analysis of malignant B cells using kappa and lambda light-chain expression along with B and T cell subset profiling showed malignant cell distributions consistent with the scRNA-seq data (Figure S2).

We obtained 73,793 CSF single cells across 21 samples from 17 patients (4 serial samples), with cell numbers ranging from 21 to 7,880 cells per sample (Figure S1B). To evaluate the sensitivity of scRNA-seq in detecting tumor cells in the CSF, we compared it to routine diagnostic parameters and cytopathology (Figure 1B; Table S1; STAR Methods). Tumor cells in GB and BrMs were identified by quantifying the expression of tumor-specific gene signatures in non-immune CSF cells[20–23] (Figure S1C). For identification of CSF tumor cells in CNSL, we computed the ratio of B cell kappa to lambda immunoglobulin chains, with monoclonality as an indicator of malignant transformation[24] (Figure S1D), consistent with flow cytometry (Figure S2C). Further, copy-number variations (CNVs) were inferred from the single-cell transcriptome genomic distribution using inferCNV (Figures S3 and S4). scRNA-seq detected tumor cells in 10 of 13 patients with CNS tumors. In contrast, cytological assessment in clinical routine diagnostics had revealed clearly neoplastic cells in CSF of eight of 12 patients and suspicious cells in five samples. Specifically, in P01, P10-T1, P12-T2, P12-T3, and P17 with unclear or negative cytopathology, we detected tumor cells by scRNA-seq. Noteworthy, we detected a low number of non-immune cells expressing an non-small cell lung cancer (NSCLC) signature and heterogeneous CNVs (Figure S3) suspicious for tumor cells in P03 with NSCLC-BrM and LMD, in line with cytopathology. These findings highlight the sensitivity of scRNA-seq to detect even low tumor cell numbers in LMD.

We next used single-cell variational inference (SCVI)[25] to integrate scRNA-seq samples to remove technical artifacts (Figure 1C). We applied clustering to assign cells the major cell types based on gene expression markers (Figures 1C and 1D). An in-depth phenotyping was conducted by further recursive clustering, resulting in a detailed annotation of the CSF cell landscape (Figure 1E). We also included 44 healthy CSF samples from a publicly available dataset (56,010 cells, Figures S1E–S1G).[18] We identified disease-specific CSF immune cell composition with a lymphoid-dominated profile in CNSL and

(C) Integrated uniform manifold approximation and projection (UMAP) of all cells in the CSF across patients and diseases (73,793 cells). Cell type color scale is the same as in (D).

(D) Barplot showing the CSF composition of the pre-treatment sample of all patients at the general resolution. Disease color scale is the same as in (B).

(E) Sankey plot of the detailed annotation of the cellular CSF landscape.

(F) Barplot showing myeloid and T cell composition across healthy and disease CSF samples. The dashed line shows the approximate clinical healthy ratio. The number of healthy samples is 44.

(G) Dotplot showing the results of applying scCODA on the general annotation comparing the disease groups against the healthy. Reference cell type used was NK cells, and the false discovery rate was set at 0.35. Only populations with significant changes are shown.

(H) Boxplots showing CD4 to CD8 ratio per patient and disease. A Wilcoxon rank-sum test was applied to compare BrMs, CNSL, and inflammatory groups against healthy. Disease color scale is the same as in (F).

(I) Heatmap showing scaled signature scores computed with a multivariate linear model on pseudo-bulked T cells or macrophages, respective of the signature, across conditions. Significant score *p* values (<0.05) are noted with asterisks.

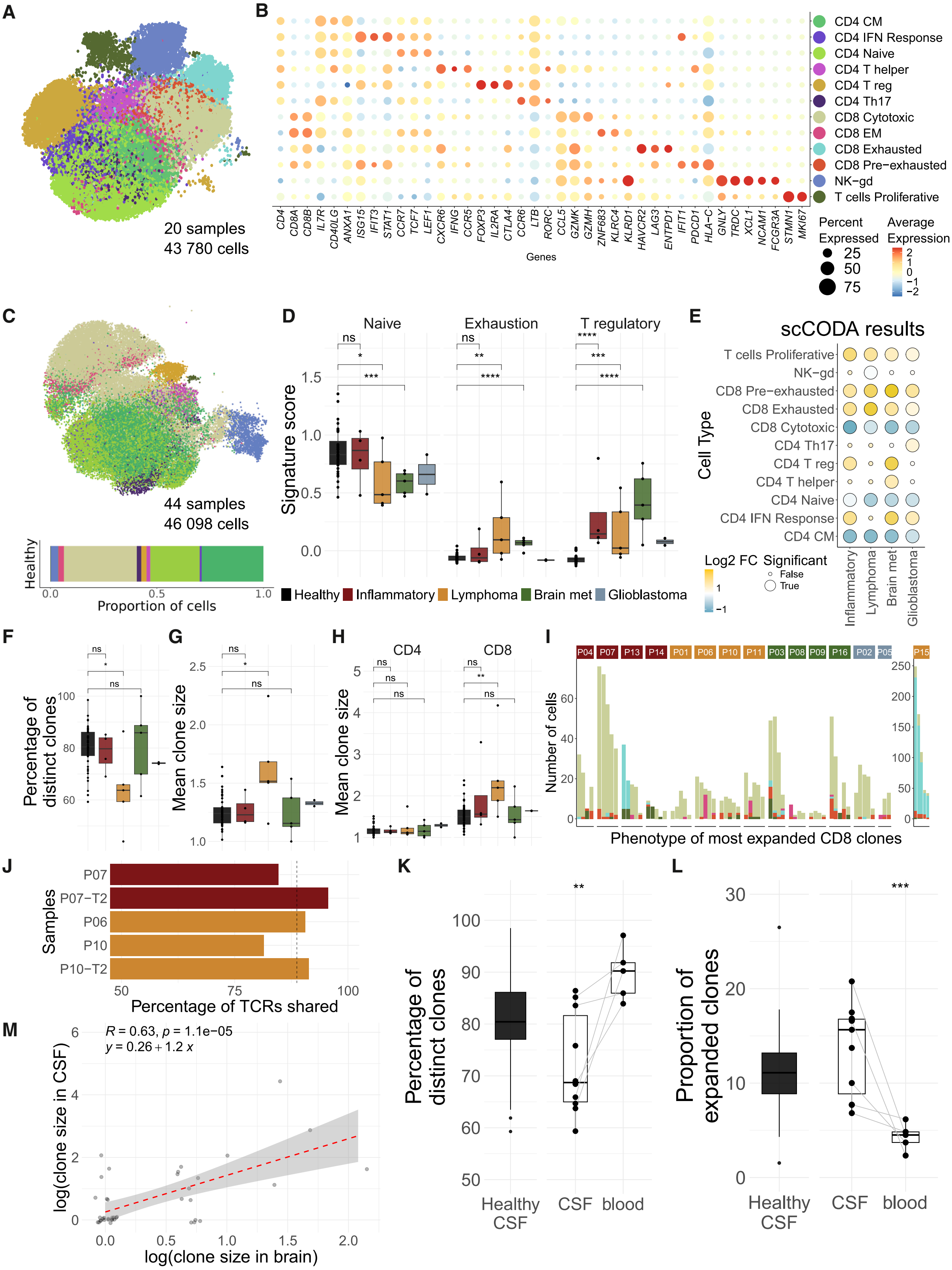

(legend on next page)

Please cite this article in press as: Nieto et al., Integrative CSF profiling identifies disease-specific immune responses in leptomeningeal disease, Cell Reports Medicine (2026), https://doi.org/10.1016/j.xcrm.2026.102651

neuro-inflammatory disorders similar to healthy CSF, in contrast to a myeloid-dominated CSF profile in GB and BrMs (Figures 1D and 1F).

To confirm disease-related CSF profiles, we performed differential cell type abundance testing of patients with CNSL, BrMs, and GB compared to patients with neuro-inflammatory diseases and healthy CSF. We confirmed a myeloid-dominated CSF profile in GB and BrMs, accompanied by a significant reduction of both CD4 and CD8 T cells as compared to healthy CSF. B cells and plasma cells increased in neuro-inflammatory pathologies and patients with GB compared to the healthy CSF (Figure 1G). The strong increase of B cells in CNSL could be explained by the infiltration of neoplastic B cells into the CSF. Patients with CNSL also showed a decrease of CD4 T cells compared to healthy CSF, in line with a significantly reduced CD4/CD8 T cell ratio compared to healthy CSF ($p = 0.012$; Figures 1G and 1H).

Given the high relevance of polarization, activation, and exhaustion for tumor pathophysiology,[26,27] respective signatures were assessed in CSF immune cells. CSF cells in neuro-inflammatory disorders showed an increase in pro-inflammatory macrophage signature (Figure 1I). In BrMs, we observed an enrichment of T cell activation and pro- and anti-inflammatory macrophages. Patients with CNSL were characterized by a strong enrichment of T cell activation and exhaustion signatures (Figure 1I), suggesting an active immune response.[18] The myeloid-dominated CSF in GB showed a mixed enrichment of pro- and anti-inflammatory macrophage signatures and a decreased T cell activation score. Together, these findings suggest that disease-specific CSF profiles reflect the respective TME.

CSF liquid biopsy captures the adaptive immune microenvironment including T cell activity

To gain a deeper understanding of the CSF T cell response, we reclustered and annotated 4,565 T cells from all samples, identifying six distinct CD4 T cells clusters including naive and memory subpopulations, T helper, and specifically Th17 and T regulatory cells (Tregs). Similarly to CNS TMEs,[28–30] we distinguished distinct CD8-exhausted populations: a terminally exhausted and a pre-exhausted subtype with lower levels of *HAVCR2*, *ENTPD1*, and *LAG3*, but high expression of *PDCD1*. We found CD8 populations, such as cytotoxic and effector memory, together with an natural killer (NK)/gamma-delta population and proliferating T cells (Figures 2A and 2B).

To investigate whether pathological conditions contribute to T cell heterogeneity among patients (Figure S5A), we projected transcriptomic profiles of T cells onto healthy CSF T cells, where we observed a predominance of naive and central memory CD4 and cytotoxic CD8 T cells (Figure 2C). Using canonical signatures of naive, Tregs, and exhausted T cells, we confirmed an increase of regulatory and exhausted phenotypes and a decrease in naive T cells in LMD (Figure 2D). Differential abundance analysis validated an increase in proliferative, pre-exhausted, and exhausted T cell subtypes compared to healthy (Figure 2E). The analysis showed an increased level of Tregs in neuro-inflammatory disorders and BrMs compared to healthy CSF (Figure 2E). Our in-depth phenotyping of CSF suggests a distinct T cell environment in the CSF of patients with CNSL, characterized by an enrichment of cytotoxic, pre-exhausted, and exhausted T cells. Clinically, the enrichment of pre-exhausted CD8 T cells in the CSF of patients with CNS tumors may represent a candidate biomarker for immunotherapy responsiveness.[28,31] In contrast, the elevated presence of Tregs in BrMs and GB suggests active suppression of anti-tumor immunity.[29,32,33]

To understand T cell activity in the CSF, we profiled the TCR repertoire, its diversity, and its expansion in CSF, through bulk deep TCR sequencing of corresponding blood samples and brain tissue (Figure S1A). Despite the heterogeneity in the repertoire size across samples (mean= 2,638.81, SD = 1,917.68,

Figure 2. CSF is a dynamic T cell environment reflecting T cell activity in CNS diseases

(A) Integrated UMAP of T cells in the CSF across patients and diseases (45,656 T cells). Cell type color scale is the same as in (B).

(B) Dotplot showing marker gene expression across T cell subpopulations. CM, central memory; IFN, interferon; EM, effector memory; NK-gd, natural killer cells and gamma-delta T cells.

(C) Integrated UMAP of T cells in healthy CSF (46,098 cells) annotated with the projected T cell subtypes in disease CSF. Barplot showing composition across all healthy samples below. Cell type color scale is the same as in (B).

(D) Boxplots showing signature scores of the main changing T cell phenotypes, computed with a multivariate linear model on pseudo-bulked T cells by patient. A Wilcoxon rank-sum test was applied to compare BrMs, CNSL, and inflammatory groups against healthy.

(E) Dotplot showing the results of applying scCODA on the T cell subtypes comparing the disease groups against the healthy. Reference cell type used was CD8 EM, and the false discovery rate was set at 0.25. Only populations with significant changes are shown.

(F) Boxplot showing TCR repertoire diversity across patients and disease by computing the percentage of distinct TCR clones by sample. A Wilcoxon rank-sum test was applied to compare the disease groups against the healthy.

(G) Boxplot showing TCR repertoire expansion across patients and disease by computing the average TCR clone size by sample. A Wilcoxon rank-sum test was applied to compare the disease groups against the healthy. Comparisons with $n < 3$ samples (GB) were not performed.

(H) Boxplot showing TCR repertoire expansion across patients and disease by computing the proportion of expanded TCR clones by sample. A TCR was considered expanded if it was found in at least 5 cells. A Wilcoxon rank-sum test was applied to compare the disease groups against the healthy.

(I) Barplot showing the top 5 most expanded CD8 TCR clones per patient and colored by the phenotype of the cells sharing each TCR. Cell type color scale is the same as in (B).

(J) Barplot showing the percentage of expanded TCR clones in the CSF found in blood for each sample. Dashed line shows the average at 88.72%.

(K) Boxplot showing TCR repertoire diversity in healthy CSF samples and disease samples with matched blood samples. A Wilcoxon rank-sum test was applied to compare the CSF and blood.

(L) Boxplot showing TCR repertoire expansion in healthy CSF samples and disease samples with matched blood samples. A TCR was considered expanded if it was found in more than one cell. A Wilcoxon rank-sum test was applied to compare the CSF and blood.

(M) Scatterplot showing logarithmic correlation between the size in brain and CSF of the 40 shared clones found.

Please cite this article in press as: Nieto et al., Integrative CSF profiling identifies disease-specific immune responses in leptomeningeal disease, Cell Reports Medicine (2026), https://doi.org/10.1016/j.xcrm.2026.102651

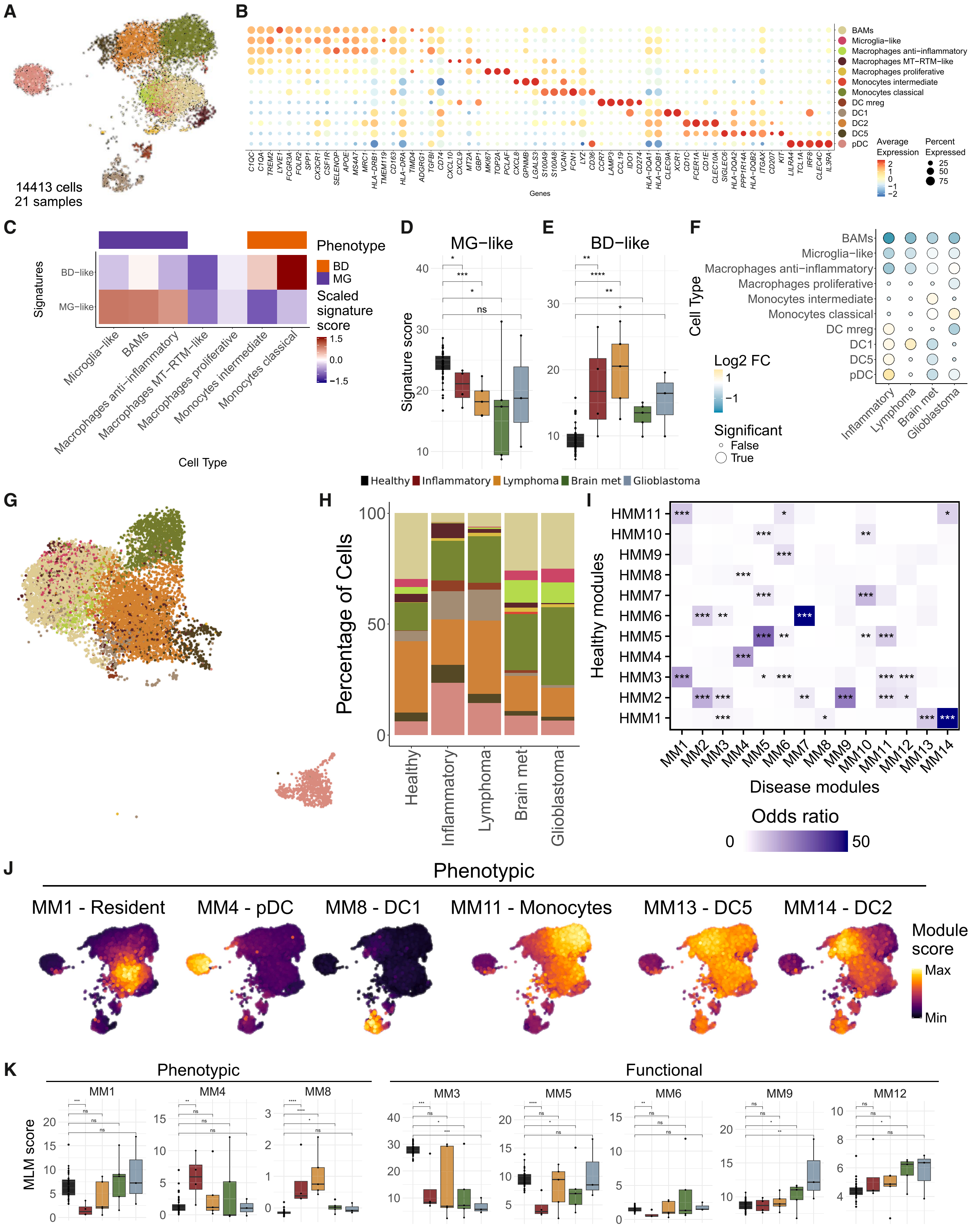

(legend on next page)

Please cite this article in press as: Nieto et al., Integrative CSF profiling identifies disease-specific immune responses in leptomeningeal disease, Cell Reports Medicine (2026), https://doi.org/10.1016/j.xcrm.2026.102651

Figure S5B), we observed a significant decrease of TCR diversity in the CSF of patients with CNSL, compared to the healthy and other disease cohorts ($p = 0.02$; Figure 2F). In line, T cell proportion of expanded clones ($p = 0.026$) and the mean clone size ($p = 0.02$) per patient were significantly higher in patients with CNSL (Figures 2G and S5C). T cell expansion in the CSF of patients with CNSL was predominantly observed in CD8 T cells, while CD4 T cells exhibited minimal expansion (Figures 2H and S5D). Therefore, we examined the phenotypes of the top five most expanded CD8 TCR clones per patient, revealing an overall expansion of predominantly cytotoxic T cells, along with smaller proportions of pre-exhausted and exhausted phenotypes (Figure 2I).

To assess whether T cell expansion occurs locally in the CSF or reflects peripheral activity, we compared TCR clones in matched CSF and blood samples (two patients with CNSL [P10 and P06] and one patient with cerebral abscess [P07], each with serial sampling). Deep TCR sequencing revealed that, on average, 88.7% of expanded CSF clones were also present in blood (Figure 2J). CSF showed greater clonal expansion and reduced TCR diversity compared to blood and healthy CSF, indicating enrichment of disease-associated T cell clones within the CSF (Figures 2K and 2I). Finally, we analyzed the overlap of TCR clones within the CSF and the brain parenchyma. Our results detected 40 T cell clones in the brain tissue that were also present in the CSF with a correlation in size in both compartments ($R = 0.63$, $p = 1.1e{-}05$) (Figure 2M).

CNS diseases modulate myeloid profiles in the CSF microenvironment

By integrating and clustering myeloid cells, we annotated 12 distinct phenotypes, including monocyte, macrophage, and dendritic cell (DC) subtypes (Figures 3A and 3B). We identified three CNS resident-like populations (border-associated macrophages [BAMs], microglia-like, and anti-inflammatory macrophages).[1,27] Conversely, we detected two monocyte populations, likely infiltrating from blood. We identified a myeloid population of mitochondrial resident tissue macrophages (MT-RTMs), recently described as resident macrophages with low levels of monocyte-related genes (resident macrophage population with high mitochondrial activity).[34] DC subsets included Mreg, DC1, DC2, DC5, and pDCs.

To explore the potential of CSF myeloid cells to acquire either blood-derived (BD) or microglia-like features in LMD subtypes, we generated transcriptional signatures representing CNS-resident (microglia-like [MG]) and BD myeloid populations.[3,35–38] These signatures were then applied to our CSF datasets to characterize the profiles of myeloid cells across conditions. We validated our signatures in external mouse and human brain single-cell datasets from Van Hove et al. 2019 and Pombo Antunes et al. 2021., confirming that the CNS-resident signatures were enriched in brain-resident compartments, whereas BD signatures marked circulating myeloid cells (Figure S6A). As an additional validation, the BD signature was consistently recapitulated in all matched blood samples, whereas the CNS-resident signature was absent (Figure S6B, all p values <0.01). The CNS-resident signature was high in three populations potentially acquiring CNS-resident transcriptional features, whereas the BD signature was enriched in two monocyte populations (Figure S3C). Both signatures helped to determine the cellular context of most populations, except MT-RTMs, previously described to derive from circulating monocytes.[34] Myeloid cells in healthy CSF showed significantly higher expression of the CNS-resident signature, in contrast to neuro-inflammatory disorders enriched in the BD signature (Figures S3D and S3E). The two signatures showed a negative correlation, indicating the predominance of an either CNS-resident or BD profile of myeloid cells ($R = -0.6$, p-value <0.01). Pathological CSF had per se more infiltration of myeloid BD cells, especially in inflammatory diseases and CNSL (Figure S6C).

Next, we projected the transcriptomic profiles of the patient cohort onto healthy controls (Figure 3G). Albeit in different proportions, all myeloid cell types from patient samples were present in healthy CSF, except for intermediate monocytes (Figure 3H). Differential abundance testing against healthy CSF confirmed a higher abundance of monocytes in patients with GB and BrM LMD (Figure 3F). Patients with BrM LMD exhibited a significant reduction in DCs in the CSF (Figure S7A). Conversely, neuro-inflammatory diseases showed an enrichment of most DC subtypes compared to healthy CSF (Figures 3F and 3H). DCs have been linked to antigen presentation, anti-tumor response, and cytotoxicity,[39,40] processes that might be disrupted in brain cancers.

To gain a deeper understanding of the functional properties of myeloid populations in the CSF, we performed network analysis to identify gene modules of highly co-expressed genes in a

Figure 3. Distinctive myeloid profiles modulate CSF milieu in CNS diseases

(A) Integrated UMAP of myeloid cells in the CSF across patients and diseases (14,413 cells). Cell type color scale is the same as in (B).

(B) Dotplot showing marker gene expression across T cell subpopulations.

(C) Heatmap showing scaled signature scores across myeloid subpopulations. MG, microglia-derived. All signature scores had a significant associated p value (>0.01).

(D and E) Boxplots showing MG and BD scores across patients and diseases. A Wilcoxon test was applied to compare BrMs, CNSL, and inflammatory groups against healthy.

(F) Dotplot showing the results of applying scCODA on the myeloid subtypes comparing the disease groups against the healthy. The reference cell type used was DC2, and the false discovery rate was set at 0.35. Only populations with significant changes are shown.

(G) Integrated UMAP of myeloid cells in healthy CSF (9,703 cells) annotated with the projected myeloid subtypes in disease CSF.

(H) Barplot showing myeloid subpopulation composition across diseases and healthy CSF.

(I) Heatmap showing gene set overlap between healthy and disease myeloid modules by computing the pairwise odds ratio. Asterisks indicate the level of significance of the associated p values: $^{*}p \leq 0.05$, $^{**}p \leq 0.01$ and $^{***}p \leq 0.001$.

(J) UMAP showing the phenotypic modules' expression on the myeloid cell populations.

(K) Boxplots showing signature scores of selected myeloid module genes across patients and conditions, computed with a multivariate linear model on pseudo-bulked myeloid cells by patient. A Wilcoxon rank-sum test was applied to compare BrMs, CNSL, and inflammatory groups against healthy.

Please cite this article in press as: Nieto et al., Integrative CSF profiling identifies disease-specific immune responses in leptomeningeal disease, Cell Reports Medicine (2026), https://doi.org/10.1016/j.xcrm.2026.102651

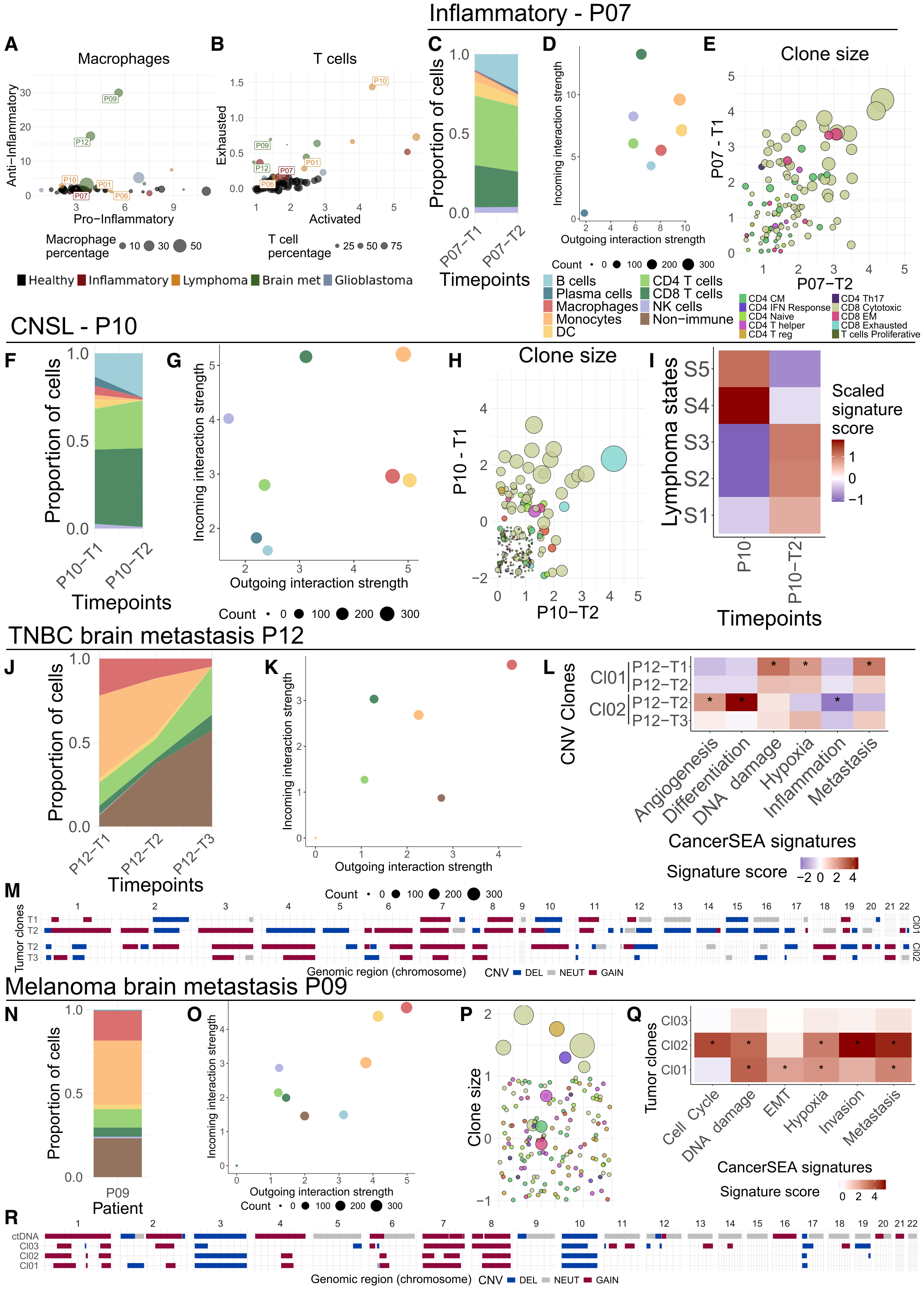

Figure 4. CSF liquid biopsy: A resource for individual disease monitoring

(A and B) Scatterplots showing the main macrophage (A) and T cell (B) signatures across all patients. Selected patients are labeled.

(C) Barplot showing population composition changes across time points of patient P07.

(legend continued on next page)

Please cite this article in press as: Nieto et al., Integrative CSF profiling identifies disease-specific immune responses in leptomeningeal disease, Cell Reports Medicine (2026), https://doi.org/10.1016/j.xcrm.2026.102651

robust and unbiased, data-driven manner (hdWGCNA, STAR Methods). We identified 11 modules for the healthy and 14 for the disease cohort (Table S2). Next, we analyzed the overlap of healthy and disease modules. All healthy modules exhibited certain similarity to disease (Figure 3I). Using this network analyses, we annotated all disease modules by an in-depth evaluation of their top hub genes (Table S3). We identified modules that specifically characterized certain phenotypes of myeloid populations, “phenotypic” modules, and others that reflected particular myeloid functions, “functional” modules (Figures 3J and S7B). Signature scoring of the top 50 genes per module revealed distinct expressions across diseases. We observed that MM1 (module 1), which characterized brain-resident populations, including BAM, MG-like, and anti-inflammatory populations, was significantly depleted in the inflammatory group compared to healthy ($p = 0.00019$) (Figures 3K, S7C, and S7D). MM4, characterizing pDCs, was significantly enriched in the inflammatory group ($p = 0.003$), confirming results of differential abundance testing (Figures 3F and 3J). MM8, which characterizes DC1, was found to be specific in BrMs and GB, which was further supported by lower DC1 cells in healthy CSF (Figures 3J, 3K, S7C, and S7D).

Also, the analysis revealed several modules indicating particular functions of the CSF myeloid cells (Figures S7B–S7E). For example, several modules indicated disease-specific metabolic shifts in CSF myeloid cells, with reduced oxidative phosphorylation (OXPHOS) (MM3) and mitochondrial activity (MM5) across LMD, particularly in BrMs, compared to healthy CSF. Glycolysis (MM6) showed no major differences between LMD subtypes but was modestly reduced overall (Figure 3K). Interestingly, MM6 module scores are positively correlated with CSF lactate levels obtained from routine clinical diagnostics (Figure S7F). Further, the MM9 module, enriched in proliferative macrophages (Figure S7D), showed a higher expression in CSF myeloid cells from patients with LMD from BrMs and GB (Figure 3K). Also, module MM12 presented interferon-related genes, suggesting that interferon signaling pathways are upregulated in patients with neuro-inflammatory disorders and CNSL (Figure 3K). Additionally, modules MM2 and MM7, associated with myeloid activation via ribosomal genes, classical HLA class I (HLA-A and HLA-C), and interferon-related genes involved in phagocytosis showed limited variation across disease types. This suggests these modules represent shared features of myeloid inflammatory activation that are consistent across patients and not disease specific (Figures S7C and S7D). Our findings suggest that CSF myeloid cells in LMD undergo metabolic reprogramming, reflecting disease-specific immune adaptation.

CSF liquid biopsy: A resource for patient-specific monitoring of disease activity and CSF immune response in LMD

Beyond LMD subtype-specific patterns, we observed patient-specific CSF immune profiles. P09 (melanoma LMD), P12 (breast cancer LMD), and P10 (CNSL LMD) showed enriched anti-inflammatory macrophages and exhausted T cells, while CNSL patient P01, responding well to treatment, exhibited pro-inflammatory macrophages and activated T cells (Figures 4A and 4B). Therefore, we conducted an in-depth analysis of patient-specific CSF profiles. The serial CSF profiling in P07 with cerebral abscess caused by bacteria exemplifies non-cancer immune response in the CSF. As shown previously, P07, displayed a T cell-driven environment (Figures 1D and 4C). Cell communication analysis showed that CD8 T cells are receiving most signals, which highlights their active role in responding to the infection (Figures 4D and S8A). Over a 2-month period of antibiotic treatment, we observed an increase of B cells as well as a reduction of DCs (Figure 4C). Further, P07 was characterized by a diverse clonal TCR expansion, especially cytotoxic CD8 T cells (Figures 4E and S8B). These findings illustrate how a resolving immune response to infection is mirrored in the CSF, culminating in full recovery.

We profiled serial CSF from P10 with aggressive CNSL and LMD. Initially, the CSF showed T cell activation and exhaustion, with elevated $CD8^+$ T cells (Figure 4B). After 1 week of steroid treatment, the relative proportions of plasma and myeloid cells declined, while the relative proportion of B cells increased, indicating steroid-induced modulation (Figures 4F and 4G). TCR analysis revealed a rapid expansion of cytotoxic and exhausted clones over the 1-week CSF profiling interval (Figure 4H). Interestingly, EcoTyper classification[41] indicated a shift from an adverse (S4–5) to a more favorable (S1–3) state of CSF lymphoma cells (Figure 4I). However, even though we could not

---

(D) Scatterplot showing incoming and outgoing interaction strength of the general populations found in the CSF of P07.

(E) Scatterplot showing TCR clone size in logarithmic scale, as well as the phenotype of the shared clones before and after treatment of CSF samples of patient P07.

(F) Barplot showing population composition changes across time points of patient P07.

(G) Scatterplot showing incoming and outgoing interaction strength of the general populations found in the CSF of P10.

(H) Scatterplot showing TCR clone size in logarithmic scale, as well as the phenotype of the shared clones before and after treatment CSF samples of patient P10. T cell phenotype color scale as in (E).

(I) Heatmap showing scaled signature scores across patient P10 samples’ B cells of the five lymphoma states from EcoTyper.

(J) Barplot showing population composition changes across time points of patient P12.

(K) Scatterplot showing incoming and outgoing interaction strength of the general populations found in the CSF of P12.

(L) Heatmap showing scaled signature scores of CancerSEA’s cancer program signatures across tumor clones and time points.

(M) Copy-number variation profiles of the two tumor clones found across all time points of patient P12.

(N) Barplot showing P09 composition.

(O) Scatterplot showing incoming and outgoing interaction strength of the general populations found in the CSF of patient P09.

(P) Scatterplot showing TCR clone size and phenotype of P09. Phenotype color scale as in (E).

(Q) Heatmap showing scaled signature scores of CancerSEA’s cancer program signatures across tumor clones of patient P09.

(R) Copy-number variation profiles of the three tumor clones found in CSF and the ctDNA profile of patient P09.

confirm the malignancy of the B cells after treatment, CNV analysis evidenced clonal differences across both time points and the relative B cell proportion did not decrease substantially despite steroid treatment in P10. Previous studies using flow cytometry have shown that steroids reduce both total myeloid and lymphoid cell numbers in the CSF.[42,43] Therefore, the relative increase in B cell proportions in P10 could also be explained by a stronger decrease in the myeloid proportions. However, the Ecotyper findings might also suggest a partial anti-tumor response, although clinical improvement after steroid treatment remained insufficient in P10.

In P12 with breast cancer BrMs and LMD, we were able to trace the evolution of a particular tumor clone during LMD progression and the development of treatment resistance. Subsequent time points showed a reduction in myeloid and an increase of tumor cells, particularly at time point 3, a progressive stage despite intrathecal methotrexate treatment (Figure 4J). Cell communication analysis revealed that macrophages modulated the CSF immune environment, while T cells showed reduced engagement in processing signals (Figure 4K). CNV analysis revealed a predominant clone (Cl01) in the first sample, characterized by gains in chromosomes 1, 7, 8, 11, and 19 and deletions in chromosomes 2, 5, 10, 15, and 19. We identified a different tumor clone (Cl02: exhibiting gains in chromosomes 3, 4, 6, 7, 8, 18, and 21 and deletions in chromosomes 1, 12, 17, and 19) in the CSF 1 week after initiation of methotrexate (T2). Cl02 became the dominant tumor cell clone at time point 3, coinciding with clinically evident disease progression (Figure 4M). Using *CancerSEA*[44] we explored the gene programs of both clones. Interestingly, clone Cl01 CSF sample displayed signatures of metastasis, hypoxia, and DNA damage and clone Cl02 shifted to signatures of differentiation and angiogenesis and a downregulation of inflammation (Figure 4L).

Next, we studied the CSF environment of P09 with advanced BRAF-mutated melanoma with BrMs and LMD (Figures 4N and S8D). Cell communication analysis confirmed that macrophages modulated the CSF environment, similar to P12 (Figure 4O). TCR analysis confirmed limited T cell anti-tumor response detected, with little clonal expansion (Figure 4P). By CNV analysis of the tumor cells, we identified three distinct clones, all of them resembling the profile of ctDNA (Figures 4R and S2). The predominant programs involved were metastasis, invasion, hypoxia, epithelial-to-mesenchymal transition, DNA damage, and cell cycle, and each clone displayed different levels of expression of these programs, with Cl02 appearing to be the most aggressive (Figure 4Q). At the time of the CSF sampling, Cl01 was the most abundant clone (Figure S8C). Moreover, we had previously identified increased BRAF signaling due to a BRAF mutation in the CSF tumor cells (Figure 1C) of this heavily pretreated P09 who previously showed resistance to BRAF/MEK and immune checkpoint inhibition.

CSF cell phenotypes mirror the immune microenvironment of CNS lesions

To explore the potential of the CSF profiling in reflecting the characteristics of parenchymal CNS lesions, we analyzed tissue sections of six patients using the Xenium spatial transcriptomics platform. Matched pairs of CSF and tissue were available for two patients with CNSL (P01 and P10), two patients with BrMs (P09 and P12), one patient with GB (P02) and one patient from the inflammatory control group (P07). We assessed the similarities in the local immune environments by spatial transcriptomics using adapted inflammation-related signatures from CSF profiling on the tissue lesions (Figure 5A). We validated our spatial transcriptomics analysis at protein level with immunohistochemical stainings of immune and tumor cells in paired brain lesions to corroborate our findings (Figure S10).

We used immuno-oncology Xenium panel genes along with CSF cell markers to identify cell types and compare the composition between CSF and tissue. We identified the main immune cell types in the tissue, including B and plasma cells, macrophages, microglia, T cells, tumor cells, neutrophils, and a heterogeneous group of non-immune cells, most likely containing neurons and other brain cell types (Figure S9A). Sample size and total cell numbers depended on available tissue samples (Figure S9B, see STAR Methods).

The tissue lesion of patient P07 (prior to antibiotic treatment) displayed a prominent presence of B and plasma cells alongside some microglia and macrophages (Figure 5B). The pro-inflammatory signature of the myeloid cells was sparse (Figure S9C). When examining the local TME of CNSL patient P01, we identified a dense accumulation of malignant B cells (Figure 5C). We also detected some activated and cytotoxic T cells (Figure S9D). Both findings were validated through immunohistochemistry with the protein expression of CD20 and the expression of CD8 (Figure S10A). CNSL P10 exhibited high concentration of malignant B cells besides accompanying plasma cells around vessel-like structures (Figure 5D). By using CXCL13 as a proxy for T cell infiltration,[45] we confirmed the co-occurrence of infiltrating T lymphocytes besides the tumor cells around vessel-like structures, which were comparable with the CD8 expression by immunohistochemistry (Figures S9E and S10B). The BrM tissue of P12 exhibited a prominent angiogenic phenotype, with numerous vessel-like structures interspersed among tumor cells (Figure 5E, regions A and B) supported by immunohistochemistry stainings (Figure S10C). Interestingly, an angiogenic phenotype was likewise identified in a CSF tumor cell clone (Cl02) emerging upon treatment resistance. Immune cell infiltration was sparse and the TME was dominated by a mix of pro- and anti-inflammatory macrophages (Figure 5A), the latter localizing predominantly around vessel-like structures. Thus, the CSF profile of P12 was similar to the tissue TME, featuring a myeloid-dominated CSF environment (Figure S9F). GB patient P02, a tumor type characterized by low immune infiltration (Figure 5F), showcased moderate levels of T cell infiltration in some regions such as around vessel-like structures (Figure S9G). This presence of T cells in the tumor tissue of P02 matches the T cell-enriched CSF, which was quite distinct from the other GB patient, P05 (for whom there's unfortunately no tissue available), who showed a T cell-depleted CSF profile. Immunohistochemistry of the brain tissue of patient P02 further confirmed the presence of T cells in the tissue (Figure S10D). The melanoma BrM tissue of P09, overall showed sparse immune infiltration, with some regions of immune activity as shown in the immunohistochemistry (Figure S10E). In a localized area, we observed a diverse infiltration of macrophages, B and plasma cells, microglia, and T cells,

Please cite this article in press as: Nieto et al., Integrative CSF profiling identifies disease-specific immune responses in leptomeningeal disease, Cell Reports Medicine (2026), https://doi.org/10.1016/j.xcrm.2026.102651

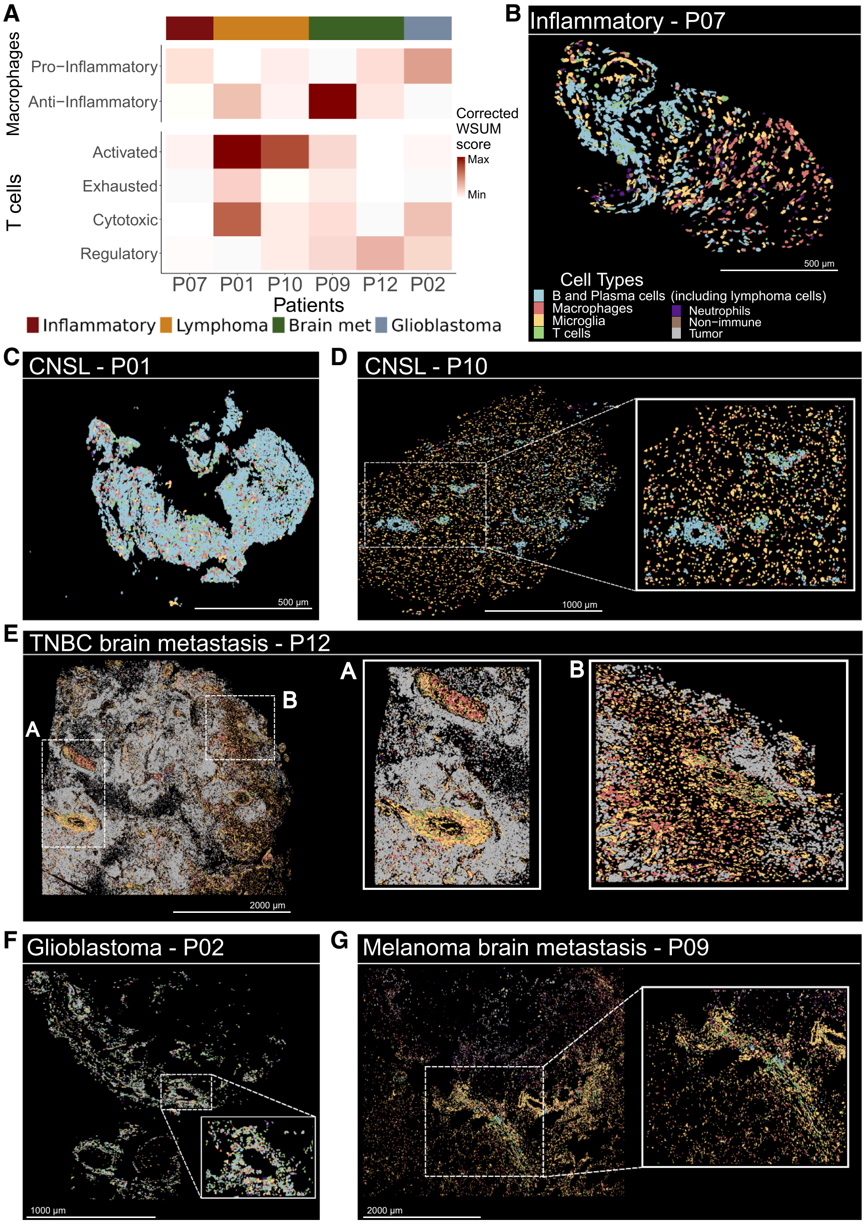

Figure 5. CSF cell phenotypes mirror the immune microenvironment of CNS diseases

(A) Heatmap showing scaled signature scores computed using corrected weighted sum, on pseudo-bulked T cells or macrophages and microglia, respective of the signature, in the brain tissue.

(B) Spatial cell type annotation of the brain tissue of inflammatory patient P07. Scale bar, 500 μm.

(C) Spatial cell type annotation of the brain tissue of CNSL patient P01. Color scale as in (B). Scale bar, 500 μm.

(D) Spatial cell type annotation of the brain tissue of CNSL patient P10, including zoomed-in region. Color scale as in (B). Scale bar, 1,000 μm.

(E) Spatial cell type annotation of the brain tissue of BrM patient P12. Two regions, labeled as A and B have been zoomed-in. Color scale as in (B). Scale bar, 2,000 μm.

(F) Spatial cell type annotation of the brain tissue of GB patient P02, including zoomed-in region. Color scale as in (B). Scale bar, 1,000 μm.

(G) Spatial cell type annotation of the brain tissue of BrM patient P09, including zoomed-in region. Color scale as in (B). Scale bar, 2,000 μm.

indicating focal immune infiltration (Figure 5G). The predominant immune cell phenotypes in the tissue are anti-inflammatory macrophages, exhibiting a predominantly myeloid controlled environment (Figure S9H).

Together, our spatial analyses demonstrate that CSF immune phenotypes often reflect the composition and activation states of tumor-infiltrating immune cells in the CNS parenchyma. P07 showed a pro-inflammatory signature in both CSF and brain tissue, while CNSL cases (P01 and P10) displayed T cell activation in tissue lesions consistent with CSF T cell profiles, although myeloid signatures diverged. BrM samples (P12 and P09) revealed sparse T cell infiltration and dominant anti-inflammatory myeloid phenotypes in both tissue and CSF; notably, P12 showed a Treg-enriched TME, while P09 exhibited localized immune infiltration. In GB patient P02, low levels of tumor-infiltrating lymphocytes mirrored a T cell-low CSF profile.

DISCUSSION

LMD is a fatal complication of advanced cancer with limited treatment options. This comprehensive multimodal analysis of patients with LMD revealed tumor type-specific immune profiles and patient-level dynamics linked to disease progression and therapy resistance. The comparison with brain lesion profiling shows that the CSF reflects key features of the TME, supporting the use of the CSF LB as a minimally invasive window into disease biology and for developing diagnostic and therapeutic strategies. While previous work has provided initial insight into the transcriptional landscape of LMD and its association with immunotherapy response, our study expands on this by combining multimodal profiling of the CSF, including scRNA-seq, TCR sequencing, and spatial transcriptomics, to capture disease-specific immune dynamics and intercompartmental interactions.[12]

The lymphoid-dominated CSF of CNSL LMD was characterized by T cell activation and TCR expansion in contrast to LMD in BrMs and GB showing a myeloid-dominated CSF. Our findings indicate T cell trafficking between blood and CSF with the majority of expanded TCR clones in CSF shared in blood. This suggests T cell expansion potentially linked to anti-tumor response especially in CNSL. Identifying shared TCRs and their

Please cite this article in press as: Nieto et al., Integrative CSF profiling identifies disease-specific immune responses in leptomeningeal disease, Cell Reports Medicine (2026), https://doi.org/10.1016/j.xcrm.2026.102651

phenotypes could pave the way for developing CSF-guided TCR cloning strategies, such as chimeric antigen receptor T cells (CAR-T cells) or TCR-based vaccines.[46,47]

In GB and BrMs, we observed a predominance of resident-like myeloid cells in CSF. In contrast, CSF from CNSL and neuroinflammatory conditions showed increased infiltration by BD myeloid cells, reflecting a peripherally driven immune response. The gene module analysis identified a metabolic shift in CSF macrophages, particularly MT-RTMs, in GB and BrMs, with elevated expression of lactate-associated programs (MM6) correlating with increased CSF lactate levels. This suggests that CSF myeloid cells may actively shape the metabolic microenvironment, with lactate serving as a potential biomarker of tumor-associated immune activity and disease progression.[48–50]

Our analysis revealed that subsets of CSF and tumor-infiltrating myeloid cells express resident-like transcriptional modules. These profiles mirror those seen in microglia and brain-resident macrophages and are consistent with reports that infiltrating bone marrow-derived macrophages can adopt resident-like phenotypes in glioma.[35,37] This suggests that the CSF may capture dynamic myeloid adaptation to the CNS environment, offering a non-invasive window into brain-compartment immune states.

Furthermore, CSF tumor cell profiling offered insights into LMD progression, as seen in P12, where serial samples revealed emerging resistance to intrathecal chemotherapy, and in P09, where tumor-immune cell interactions may explain resistance to immune checkpoint inhibitors. These findings highlight the need to generate resources that could help to explain both disease-associated and patient-specific mechanisms, with implications for personalized therapies and clinical trial design.[51] These exploratory, multimodal findings provide a valuable foundation for future studies in LMD. CSF profiling reveals patient-specific immune states and may enable immune-based stratification and early detection of treatment resistance.

Limitations of the study

This study has several limitations. Although it represents one of the most comprehensive scRNA-seq datasets of CSF from patients with LMD to date[12,18,19,52–54] and integrates multiple layers, including scRNA-seq, scTCR-seq, deep TCR-seq, and spatial transcriptomics, the study is limited by its exploratory, non-randomized, retrospective design and modest cohort size and the data have to be interpreted with caution in this regard. In addition, the data are primarily descriptive, as mechanistic validation or lineage-tracing experiments were not feasible within the scope of this study. More generally, CSF LB enables minimally invasive profiling of immune responses and disease dynamics in CNS tumors, particularly LMD, but currently serves as a complement to, rather than a substitute for, tissue-based analyses in patients with brain tumors. Further, similar to other pilot studies on emerging CSF LB technologies, this work is limited by the lack of standardization and methodological harmonization required for clinical translation. Larger, independent, and prospective studies with standardized CSF sampling at defined time points will be essential to establish the robustness and clinical utility of scRNA-seq-based CSF profiling.

RESOURCE AVAILABILITY

Lead contact

For additional information regarding resources, kindly direct your correspondence to the lead contact, Juan C. Nieto (juan.nieto@cnag.eu).

Materials availability

This study did not generate new unique reagents.

Data and code availability

- Raw single-cell RNA and TCR sequencing data (fastq files) of CSF samples are deposited in GEO (GSE286518).
- Xenium spatial transcriptomics raw data are deposited in Zenodo (https://doi.org/10.5281/zenodo.14510199).
- Access and exploration of processed CSF data are available through the CELLxGENE portal (https://cellxgene.cziscience.com/collections/573e2e06-8af0-4d96-bfdd-7d64a4bb9c21).
- All code, scripts, and notebooks related to this publication are available on GitHub (https://github.com/Single-Cell-Genomics-Group-CNAG-CRG/CSF).
- All data and code are publicly available as of the date of publication. Additional information is available upon reasonable request to the lead contact.

ACKNOWLEDGMENTS

S.K. received intramural funding from the medical faculty of the Goethe University (Frankfurt Research Funding “Junior Clinician Scientist” program) as well as within the INDEEP “Clinician Scientist” program (Deutsche Forschungsgemeinschaft). K.J.W. and M.D. received intramural grants from the Goethe University (Frankfurt research funding). P.S.Z. and K.J.W. were funded by the Mildred Scheel Career Center Frankfurt (Deutsche Krebshilfe/German Cancer Aid). Research of P.S.Z. and J.P.S. is supported by the Ministry of Higher Education, Research and the Arts of the State of Hesse (HMWK), within the LOEWE Center Frankfurt Cancer Institute (FCI). The Dr. Senckenberg Institute of Neurooncology is supported by the Dr. Senckenberg Foundation. P.N. holds an FPI PhD fellowship from the Spanish Universities Ministry. We acknowledge funding from the European Union’s H2020 research and innovation program (grant agreement 848028) and from the European Research Council (ERC) under the European Union’s Horizon 2020 Research and Innovation Program (grant agreement 810287) awarded to H.H. Further support to H.H. was received from the Ministerio de Ciencia e Innovación (MCI) under grant agreements PID2020-115439GB-I00, PID2023 -148687OB-I00, and PID2024-161652OB-I00 and PLEC2021-007654, and by ERA-NET Neuron/Ministerio de Ciencia e Innovación (MCI) under grant agreement PCI2022-133012. H.H. has received additional funding from the European Union’s Horizon Europe Research and Innovation program (grant agreement 101072891) and from LaCaixa Foundation (grants HR22-0031 and HR22-0172). We are also thankful to the Generalitat de Catalunya through the Suport Grups deRecerca AGAUR (2021-SGR2021-01216 to H.H.). This work was also supported by an ASPIRE Award from The Mark Foundation for Cancer Research and the Scientific Foundation of the Spanish Association Against Cancer (CATALYST 0000000014). All patients included in the study gave consent toward biomaterial collection and analyses. The study protocol was approved by the ethical committee of the medical faculty of the Goethe University Frankfurt, Germany (SNO-9-2022). We thank the UCT Biobank and Tumor Documentation as part of the interdisciplinary Biobank and Database Frankfurt (iBDF) for their valuable support in biomaterial and patient data management. We thank the patients and their families, without whom this research would not have been possible.

AUTHOR CONTRIBUTIONS

Conceived the study, H.H., P.S.Z., and J.C.N.; study design, P.N., H.H., P.S.Z., and J.C.N.; supervised the project, H.H., P.S.Z., and J.C.N.; carried out CSF and PBMC sample acquisition and cryopreservation, P.S.Z., S.K., and M.D.;

Please cite this article in press as: Nieto et al., Integrative CSF profiling identifies disease-specific immune responses in leptomeningeal disease, Cell Reports Medicine (2026), https://doi.org/10.1016/j.xcrm.2026.102651

immune cell annotation, J.C.N.; provided and analyzed biomaterial (tissue and/or CSF) and clinical data of the patients, P.S.Z., S.K., K.J.W., M.C., K.H.P., and P.N.H.; performed single-cell RNA sequencing experiments, P.S.Z., G.C., D.M., and J.C.N.; annotated lesion areas of brain samples, K.J.W. and A.P.R.; cut the brain samples, M.A.V. and S.V.; performed Xenium experiments, A.P.-R., P.L., and I.R.; performed, analyzed, and/or supervised Nanopore sequencing of cell-free DNA, S.K., M.D., P.S.Z., P.N.H., K.I., and P.E.; processed OS-TCR data, J.L.M.; performed the bioinformatic analyses of single-cell and spatial data, P.N.; performed the network analysis, S.M.; provided equipment, P.S.Z., K.H.P., J.P.S., and H.H.; interpreted the results and drafted the manuscript, P.N., H.H., P.S.Z., and J.C.N.; all authors contributed valuable critical discussion to the writing of the manuscript and read and approved the final version.

DECLARATION OF INTERESTS

J.P.S. has received honoraria for lectures, advisory board participation, consulting, and travel grants from Abbvie, Roche, Boehringer, Bristol-Myers Squibb, Medac, Mundipharma, and UCB unrelated to this study. P.S.Z. has received a lecture honorarium from Bristol-Myers Squibb unrelated to this study. H.H. is co-founder and shareholder of Omniscope, scientific advisory board member of Nanostring and MiRXES, and consultant to Moderna and Singularity. J.C.N. is a scientific consultant to Omniscope.

STAR★METHODS

Detailed methods are provided in the online version of this paper and include the following:

- KEY RESOURCES TABLE
- METHOD DETAILS
    - Experimental model and study participant details (STAR Methods)
    - Immunohistochemistry (IHC)
    - Collection and cryopreservation of cells from cerebrospinal fluid and peripheral blood mononuclear cells
    - Single cell RNA-sequencing
    - Nanopore-sequencing of cell-free DNA from cerebrospinal fluid
    - Xenium In Situ analyzer
- QUANTIFICATION AND STATISTICAL ANALYSIS (STAR METHODS)
    - scRNA-seq data pre-processing and quality control
    - Healthy cohort
    - Normalization and clustering
    - General annotation
    - Integration and in-depth annotation
    - Tumor cell identification in CSF scRNA-seq
    - TCR data analysis
    - Signature scoring and pseudobulk analysis
    - Compositional analysis
    - Gene co-expression network analysis
    - Cell communication analysis
    - Xenium data analysis
    - Statistical analysis and data visualization
    - Boxplots

SUPPLEMENTAL INFORMATION

Supplemental information can be found online at https://doi.org/10.1016/j.xcrm.2026.102651.

Received: August 13, 2025
Revised: December 2, 2025
Accepted: February 3, 2026

REFERENCES

1. Munro, D.A.D., Movahedi, K., and Priller, J. (2022). Macrophage compartmentalization in the brain and cerebrospinal fluid system. Sci. Immunol. *7*, eabk0391.
2. Croese, T., Castellani, G., and Schwartz, M. (2021). Immune cell compartmentalization for brain surveillance and protection. Nat. Immunol. *22*, 1083–1092.
3. Friebel, E., Kapolou, K., Unger, S., Núñez, N.G., Utz, S., Rushing, E.J., Regli, L., Weller, M., Greter, M., Tugues, S., et al. (2020). Single-Cell Mapping of Human Brain Cancer Reveals Tumor-Specific Instruction of Tissue-Invading Leukocytes. Cell *181*, 1626–1642.e20. https://doi.org/10.1016/j.cell.2020.04.055.
4. Zeiner, P.S., Preusse, C., Golebiewska, A., Zinke, J., Iriondo, A., Muller, A., Kaoma, T., Filipski, K., Müller-Eschner, M., Bernatz, S., et al. (2019). Distribution and prognostic impact of microglia/macrophage subpopulations in gliomas. Brain Pathol. *29*, 513–529.
5. Bagley, S.J., Logun, M., Fraietta, J.A., Wang, X., Desai, A.S., Bagley, L.J., Nabavizadeh, A., Jarocha, D., Martins, R., Maloney, E., et al. (2024). Intrathecal bivalent CAR T cells targeting EGFR and IL13Rα2 in recurrent glioblastoma: phase 1 trial interim results. Nat. Med. *30*, 1320–1329. https://doi.org/10.1038/s41591-024-02893-z.
6. Nayak, L., Bettegowda, C., Scherer, F., Galldiks, N., Ahluwalia, M., Baraniskin, A., von Baumgarten, L., Bromberg, J.E.C., Ferreri, A.J.M., Grommes, C., et al. (2024). Liquid biopsy for improving diagnosis and monitoring of CNS lymphomas: A RANO review. Neuro Oncol. *26*, 993–1011.
7. Tawbi, H.A., Forsyth, P.A., Hodi, F.S., Algazi, A.P., Hamid, O., Lao, C.D., Moschos, S.J., Atkins, M.B., Lewis, K., Postow, M.A., et al. (2021). Long-term outcomes of patients with active melanoma brain metastases treated with combination nivolumab plus ipilimumab (CheckMate 204): final results of an open-label, multicentre, phase 2 study. Lancet Oncol. *0*.
8. Nadal, E., Rodríguez-Abreu, D., Simó, M., Massutí, B., Juan, O., Huidobro, G., López, R., De Castro, J., Estival, A., Mosquera, J., et al. (2023). Phase II Trial of Atezolizumab Combined With Carboplatin and Pemetrexed for Patients With Advanced Nonsquamous Non-Small-Cell Lung Cancer With Untreated Brain Metastases (Atezo-Brain, GECP17/05). J. Clin. Oncol. *41*, 4478–4485.
9. Le Rhun, E., Weller, M., van den Bent, M., Brandsma, D., Furtner, J., Rudà, R., Schadendorf, D., Seoane, J., Tonn, J.C., Wesseling, P., et al. (2023). Leptomeningeal metastasis from solid tumours: EANO-ESMO Clinical Practice Guideline for diagnosis, treatment and follow-up. ESMO Open *8*, 101624.
10. Schorb, E., Isbell, L.K., Kerkhoff, A., Mathas, S., Braulke, F., Egerer, G., Röth, A., Schliffke, S., Borchmann, P., Brunnberg, U., et al. (2024). High-dose chemotherapy and autologous haematopoietic stem-cell transplantation in older, fit patients with primary diffuse large B-cell CNS lymphoma (MARTA): a single-arm, phase 2 trial. Lancet Haematol. *11*, e196–e205.
11. Remsik, J., and Boire, A. (2024). The path to leptomeningeal metastasis. Nat. Rev. Cancer *24*, 448–460.
12. Prakadan, S.M., Alvarez-Breckenridge, C.A., Markson, S.C., Kim, A.E., Klein, R.H., Nayyar, N., Navia, A.W., Kuter, B.M., Kolb, K.E., Bihun, I., et al. (2021). Genomic and transcriptomic correlates of immunotherapy response within the tumor microenvironment of leptomeningeal metastases. Nat. Commun. *12*, 5955.
13. Boire, A., Brandsma, D., Brastianos, P.K., Le Rhun, E., Ahluwalia, M., Junck, L., Glantz, M., Groves, M.D., Lee, E.Q., Lin, N., et al. (2019). Liquid biopsy in central nervous system metastases: a RANO review and proposals for clinical applications. Neuro Oncol. *21*, 571–584.
14. Glass, D.R., Tsai, A.G., Oliveria, J.P., Hartmann, F.J., Kimmey, S.C., Calderon, A.A., Borges, L., Glass, M.C., Wagar, L.E., Davis, M.M., and Bendall, S.C. (2020). An Integrated Multi-omic Single-Cell Atlas of Human B Cell Identity. Immunity *53*, 217–232.e5.

15. Nieto, P., Elosua-Bayes, M., Trincado, J.L., Marchese, D., Massoni-Badosa, R., Salvany, M., Henriques, A., Nieto, J., Aguilar-Fernández, S., Mereu, E., et al. (2021). A single-cell tumor immune atlas for precision oncology. Genome Res. *31*, 1913–1926.

16. Ruiz-Moreno, C., Salas, S.M., Samuelsson, E., Minaeva, M., Ibarra, I., Grillo, M., Brandner, S., Roy, A., Forsberg-Nilsson, K., Kranendonk, M.E.G., et al. (2025). Charting the single-cell and spatial landscape of IDH-wild-type glioblastoma with GBmap. Neuro Oncol. *27*, 2281–2295. https://doi.org/10.1093/neuonc/noaf113.

17. Alcantara, M., Fuentealba, J., and Soussain, C. (2021). Emerging Landscape of Immunotherapy for Primary Central Nervous System Lymphoma. Cancers *13*, 5061.

18. Piehl, N., van Olst, L., Ramakrishnan, A., Teregulova, V., Simonton, B., Zhang, Z., Tapp, E., Channappa, D., Oh, H., Losada, P.M., et al. (2022). Cerebrospinal fluid immune dysregulation during healthy brain aging and cognitive impairment. Cell *185*, 5028–5039.e13.

19. Rubio-Perez, C., Planas-Rigol, E., Trincado, J.L., Bonfill-Teixidor, E., Arias, A., Marchese, D., Moutinho, C., Serna, G., Pedrosa, L., Iurlaro, R., et al. (2021). Immune cell profiling of the cerebrospinal fluid enables the characterization of the brain metastasis microenvironment. Nat. Commun. *12*, 1503.

20. Lu, C.-H., Wei, S.T., Liu, J.J., Chang, Y.J., Lin, Y.F., Yu, C.S., and Chang, S.L.Y. (2022). Recognition of a Novel Gene Signature for Human Glioblastoma. Int. J. Mol. Sci. *23*, 4157.

21. Zeng, C., Lin, M., Jin, Y., and Zhang, J. (2022). Identification of Key Genes Associated with Brain Metastasis from Breast Cancer: A Bioinformatics Analysis. Med. Sci. Monit. *28*, e935071.

22. Sultana, A., Alam, M.S., Liu, X., Sharma, R., Singla, R.K., Gundamaraju, R., and Shen, B. (2023). Single-cell RNA-seq analysis to identify potential biomarkers for diagnosis, and prognosis of non-small cell lung cancer by using comprehensive bioinformatics approaches. Transl. Oncol. *27*, 101571.

23. Lee, J.Y., Park, K., Lee, E., Ahn, T., Jung, H.H., Lim, S.H., Hong, M., Do, I.G., Cho, E.Y., Kim, D.H., et al. (2016). Gene Expression Profiling of Breast Cancer Brain Metastasis. Sci. Rep. *6*, 28623.

24. Zhao, Y., Xu, H., Zhang, M., and Li, L. (2022). Single-Cell RNA-Seq and Bulk RNA-Seq Reveal Intratumoral Heterogeneity and Tumor Microenvironment Characteristics in Diffuse Large B-Cell Lymphoma. Front. Genet. *13*, 881345.

25. Gayoso, A., Lopez, R., Xing, G., Boyeau, P., Valiollah Pour Amiri, V., Hong, J., Wu, K., Jayasuriya, M., Mehlman, E., Langevin, M., et al. (2022). A Python library for probabilistic analysis of single-cell omics data. Nat. Biotechnol. *40*, 163–166.

26. Watowich, M.B., Gilbert, M.R., and Larion, M. (2023). T cell exhaustion in malignant gliomas. Trends Cancer *9*, 270–292.

27. Blanco-Carmona, E., Narayanan, A., Hernandez, I., Nieto, J.C., Elosua-Bayes, M., Sun, X., Schmidt, C., Pamir, N., Özduman, K., Herold-Mende, C., et al. (2023). Tumor heterogeneity and tumor-microglia interactions in primary and recurrent IDH1-mutant gliomas. Cell Rep. Med. *4*, 101249.

28. Brunell, A.E., Lahesmaa, R., Autio, A., and Thotakura, A.K. (2023). Exhausted T cells hijacking the cancer-immunity cycle: Assets and liabilities. Front. Immunol. *14*, 1151632.

29. Togashi, Y., Shitara, K., and Nishikawa, H. (2019). Regulatory T cells in cancer immunosuppression — implications for anticancer therapy. Nat. Rev. Clin. Oncol. *16*, 356–371.

30. Masopust, D., Awasthi, A., Bosselut, R., Brooks, D.G., Buggert, M., Chamoto, K., Cui, W., Dong, C., Farber, D.L., Gebhardt, T., et al. (2025). Guidelines for T cell nomenclature. Nat. Rev. Immunol., 1–16. https://doi.org/10.1038/s41577-025-01238-2.

31. Hu, J., Han, C., Zhong, J., Liu, H., Liu, R., Luo, W., Chen, P., and Ling, F. (2021). Dynamic Network Biomarker of Pre-Exhausted CD8+ T Cells Contributed to T Cell Exhaustion in Colorectal Cancer. Front. Immunol. *12*, 691142.

32. Mazet, J.M., Mahale, J.N., Tong, O., Watson, R.A., Lechuga-Vieco, A.V., Pirgova, G., Lau, V.W.C., Attar, M., Koneva, L.A., Sansom, S.N., et al. (2023). IFNγ signaling in cytotoxic T cells restricts anti-tumor responses by inhibiting the maintenance and diversity of intra-tumoral stem-like T cells. Nat. Commun. *14*, 321.

33. Sevenich, L. (2019). Turning "Cold" Into "Hot" Tumors—Opportunities and Challenges for Radio-Immunotherapy Against Primary and Metastatic Brain Cancers. Front. Oncol. *9*, 163.

34. Ma, R.-Y., Black, A., and Qian, B.-Z. (2022). Macrophage diversity in cancer revisited in the era of single-cell omics. Trends Immunol. *43*, 546–563.

35. Bowman, R.L., Klemm, F., Akkari, L., Pyonteck, S.M., Sevenich, L., Quail, D.F., Dhara, S., Simpson, K., Gardner, E.E., Iacobuzio-Donahue, C.A., et al. (2016). Macrophage Ontogeny Underlies Differences in Tumor-Specific Education in Brain Malignancies. Cell Rep. *17*, 2445–2459. https://doi.org/10.1016/j.celrep.2016.10.052.

36. Klemm, F., Maas, R.R., Bowman, R.L., Kornete, M., Soukup, K., Nassiri, S., Brouland, J.P., Iacobuzio-Donahue, C.A., Brennan, C., Tabar, V., et al. (2020). Interrogation of the Microenvironmental Landscape in Brain Tumors Reveals Disease-Specific Alterations of Immune Cells. Cell *181*, 1643–1660.e17. https://doi.org/10.1016/j.cell.2020.05.007.

37. Van Hove, H., Martens, L., Scheyltjens, I., De Vlaminck, K., Pombo Antunes, A.R., De Prijck, S., Vandamme, N., De Schepper, S., Van Isterdael, G., Scott, C.L., et al. (2019). A single-cell atlas of mouse brain macrophages reveals unique transcriptional identities shaped by ontogeny and tissue environment. Nat. Neurosci. *22*, 1021–1035.

38. Immune Cells and CNS Physiology: Microglia and beyond | Journal of Experimental Medicine | Rockefeller University Press. https://rupress.org/jem/article/216/1/60/42423/Immune-cells-and-CNS-physiology-Microglia-and.

39. Ferris, S.T., Durai, V., Wu, R., Theisen, D.J., Ward, J.P., Bern, M.D., Davidson, J.T., 4th, Bagadia, P., Liu, T., Briseño, C.G., et al. (2020). cDC1 prime and are licensed by CD4+ T cells to induce anti-tumour immunity. Nature *584*, 624–629.

40. Hongo, D., Zheng, P., Dutt, S., Pawar, R.D., Meyer, E., Engleman, E.G., and Strober, S. (2021). Identification of Two Subsets of Murine DC1 Dendritic Cells That Differ by Surface Phenotype, Gene Expression, and Function. Front. Immunol. *12*, 746469.

41. Steen, C.B., Luca, B.A., Esfahani, M.S., Azizi, A., Sworder, B.J., Nabet, B.Y., Kurtz, D.M., Liu, C.L., Khameneh, F., Advani, R.H., et al. (2021). The landscape of tumor cell states and ecosystems in diffuse large B cell lymphoma. Cancer Cell *39*, 1422–1437.e10.

42. Durelli, L., Poccardi, G., and Cavallo, R. (1991). CD8+ high CD11b+ low T cells (T suppressor-effectors) in multiple sclerosis cerebrospinal fluid are increased during high dose corticosteroid treatment. J. Neuroimmunol. *31*, 221–228.

43. Höpner, L., Proschmann, U., Inojosa, H., Ziemssen, T., and Akgün, K. (2024). Corticosteroid-depending effects on peripheral immune cell subsets vary according to disease modifying strategies in multiple sclerosis. Front. Immunol. *15*, 1404316.

44. CancerSEA: a cancer single-cell state atlas | Nucleic Acids Research | Oxford Academic. https://academic.oup.com/nar/article/47/D1/D900/5133662.

45. Tan, C.L., Lindner, K., Boschert, T., Meng, Z., Rodriguez Ehrenfried, A., De Roia, A., Haltenhof, G., Faenza, A., Imperatore, F., Bunse, L., et al. (2025). Prediction of tumor-reactive T cell receptors from scRNA-seq data for personalized T cell therapy. Nat. Biotechnol. *43*, 134–142. https://doi.org/10.1038/s41587-024-02161-y.

46. Choquet, S., Soussain, C., Azar, N., Morel, V., Metz, C., Ursu, R., Waultier-Rascalou, A., di Blasi, R., Houot, R., Souchet, L., et al. (2024). CAR T-cell therapy induces a high rate of prolonged remission in relapsed primary CNS lymphoma: Real-life results of the LOC network. Am. J. Hematol. *99*, 1240–1249.

47. Frigault, M.J., Dietrich, J., Gallagher, K., Roschewski, M., Jordan, J.T., Forst, D., Plotkin, S.R., Cook, D., Casey, K.S., Lindell, K.A., et al. (2022).

Please cite this article in press as: Nieto et al., Integrative CSF profiling identifies disease-specific immune responses in leptomeningeal disease, Cell Reports Medicine (2026), https://doi.org/10.1016/j.xcrm.2026.102651

Safety and efficacy of tisagenlecleucel in primary CNS lymphoma: a phase 1/2 clinical trial. Blood *139*, 2306–2315.

48. Hanahan, D. (2022). Hallmarks of Cancer: New Dimensions. Cancer Discov. *12*, 31–46.
49. Understanding the Warburg Effect: The Metabolic Requirements of Cell Proliferation | Science. https://www.science.org/doi/10.1126/science.1160809.
50. Khan, F., Lin, Y., Ali, H., Pang, L., Dunterman, M., Hsu, W.H., Frenis, K., Grant Rowe, R., Wainwright, D.A., McCortney, K., et al. (2024). Lactate dehydrogenase A regulates tumor-macrophage symbiosis to promote glioblastoma progression. Nat. Commun. *15*, 1987.
51. Sener, U., Wilcox, J.A., and Boire, A.A. (2025). Leptomeningeal Disease: Current Approaches and Future Directions. Curr. Neurol. Neurosci. Rep. *25*, 25.
52. Remsik, J., Tong, X., Kunes, R.Z., Li, M.J., Estrera, R., Snyder, J., Thomson, C., Osman, A.M., Chabot, K., Sener, U.T., et al. (2025). Interferon-γ orchestrates leptomeningeal anti-tumour response. Nature *643*, 1087–1096.
53. Smalley, I., Chen, Z., Phadke, M., Li, J., Yu, X., Wyatt, C., Evernden, B., Messina, J.L., Sarnaik, A., Sondak, V.K., et al. (2021). Single cell characterization of the immune microenvironment of melanoma brain and leptomeningeal metastases. Clin. Cancer Res. *27*, 4109–4125.
54. Chi, Y., Remsik, J., Kiseliovas, V., Derderian, C., Sener, U., Alghader, M., Saadeh, F., Nikishina, K., Bale, T., Iacobuzio-Donahue, C., et al. (2020). Cancer cells deploy lipocalin-2 to collect limiting iron in leptomeningeal metastasis. Science *369*, 276–282.
55. Yang, Q., Safina, K.R., Nguyen, K.D.Q., and Tuong, Z.K. (2025). Borcherding N. scRepertoire 2: Enhanced and efficient toolkit for single-cell immune profiling. PLoS Comput Biol *21*, e1012760. https://doi.org/10.1371/journal.pcbi.1012760.
56. Büttner M., Ostner J., Müller C.L., Theis F.J., Schubert B. scCODA is a Bayesian model for compositional single-cell data analysis. Nat Commun. 2021 Nov 25;12:6876. doi: 10.1038/s41467-021-27150-6.
57. Miyoshi, E., Morabito, S., Henningfield, C.M., Das, S., Rahimzadeh, N., Shabestari, S.K., Michael, N., Emerson, N., Reese, F., Shi, Z., et al. (2024). Spatial and single-nucleus transcriptomic analysis of genetic and sporadic forms of Alzheimer's disease. Nat Genet *56*, 2704–2717. https://doi.org/10.1038/s41588-024-01961-x.
58. Shen L., Sinai ISoMaM (2025). GeneOverlap: Test and visualize gene overlaps. doi:10.18129/B9.bioc.GeneOverlap, R package version 1.46.0, https://bioconductor.org/packages/GeneOverlap.
59. Jin, S., Plikus, M.V., and Nie, Q. (2025). CellChat for systematic analysis of cell-cell communication from single-cell transcriptomics. Nat Protoc *20*, 180–219. https://doi.org/10.1038/s41596-024-01045-4.
60. Bravo González-Blas, C., Quan, X.J., Duran-Romaña, R., Taskiran, I.I., Koldere, D., Davie, K., Christiaens, V., Makhzami, S., Hulselmans, G., de Waegeneer, M., et al. (2020). Identification of genomic enhancers through spatial integration of single-cell transcriptomics and epigenomics. Mol Syst Biol *16*, e9438. https://doi.org/10.15252/msb.20209438.
61. Rhun, E.L., Weller, M., van den Bent, M., Brandsma, D., Furtner, J., Rudà, R., Schadendorf, D., Seoane, J., Tonn, J.C., Wesseling, P., et al. (2023). Leptomeningeal metastasis from solid tumours: EANO–ESMO Clinical Practice Guideline for diagnosis, treatment and follow-up. ESMO Open *8*, 101624.
62. Yuan, D., Jugas, R., Pokorna, P., Sterba, J., Slaby, O., Schmid, S., Siewert, C., Osberg, B., Capper, D., Halldorsson, S., et al. (2025). crossNN is an explainable framework for cross-platform DNA methylation-based classification of tumors. Nat. Cancer *6*, 1283–1294.
63. Euskirchen, P., Bielle, F., Labreche, K., Kloosterman, W.P., Rosenberg, S., Daniau, M., Schmitt, C., Masliah-Planchon, J., Bourdeaut, F., Dehais, C., et al. (2017). Same-day genomic and epigenomic diagnosis of brain tumors using real-time nanopore sequencing. Acta Neuropathol. *134*, 691–703.
64. Shen, L. & Icahn School of Medicine at Mount Sinai GeneOverlap. (2023). Test and Visualize Gene Overlaps. https://doi.org/10.18129/B9.bioc.GeneOverlap.

Please cite this article in press as: Nieto et al., Integrative CSF profiling identifies disease-specific immune responses in leptomeningeal disease, Cell Reports Medicine (2026), https://doi.org/10.1016/j.xcrm.2026.102651

STAR★METHODS

KEY RESOURCES TABLE

REAGENT or RESOURCE	SOURCE	IDENTIFIER
Deposited data		
Raw single-cell RNA and TCR data	This study	GSE286518
Raw spatial transcriptomics data	This study	https://doi.org/10.5281/zenodo.14510199
Processed CSF data	This study	https://cellxgene.cziscience.com/collections/573e2e06-8af0-4d96-bfdd-7d64a4bb9c21
Software and algorithms		
CellRanger (version 7.0.0)	10X Genomics	https://www.10xgenomics.com/support/software/cell-ranger/7.2
R versions 4.2.3 (2023-03-15) and 4.3.3 (2024-02-29)	R Core Team 2021	https://www.R-project.org/
Python version 3.8.5	Python Software Foundation	https://www.python.org/
Seurat R package (version 5.1.0)	Satija Lab	https://satijalab.org/seurat/
Scrublet package	–	https://github.com/swolock/scrublet
scVI python package (version 1.0.4)	Yosef Lab	https://scvi-tools.org/
scanpy python package (version 1.9.6)	–	https://scanpy.readthedocs.io/en/stable/
inferCNV R package (version 1.3.3)	Trinity CTAT Project	https://github.com/broadinstitute/inferCNV
scRepertoire R package (version 1.12.0)	Yang et al.[55]	https://www.bioconductor.org/packages/release/bioc/html/scRepertoire.html
UCell R package (version 2.6.2)	Andreatta and Carmona (2021)	https://bioconductor.org/packages/release/bioc/html/UCell.html
presto R package (version 1.0.0)	Raychaudhuri Lab	https://github.com/immunogenomics/presto
decoupleR R package (version 2.8.0)	Saez Lab	https://saezlab.github.io/decoupleR/
scCODA Python package	Büttner and Ostner et al. (2021)[56]	https://pypi.org/project/scCODA/
hdWGCNA R package (version 0.4.0)	Miyoshi et al. (2024)[57]	https://smorabit.github.io/hdWGCNA/
GeneOverlap R package (version 1.38.0)	Shen and Sinai (2025)[58]	https://bioconductor.org/packages/release/bioc/html/GeneOverlap.html
CellChat R package (version 2.1.2)	Suoqin Jin et al. (2024)[59]	https://github.com/jinworks/CellChat
AUCell R package (version 1.24.0)	Bravo González-Blas et al.[60]	https://bioconductor.org/packages/release/bioc/html/AUCell.html
Other		
Biorender	–	https://www.biorender.com/
Inkscape	–	https://inkscape.app/
Code repository	This study	https://github.com/Single-Cell-Genomics-Group-CNAG-CRG/CSF

METHOD DETAILS

Experimental model and study participant details (STAR Methods)

The patient cohort comprises scRNA-seq data from 20 CSF samples retrospectively collected from 16 patients (Figure 1; Table S1). Inclusion criteria for the 12 patients with CNS neoplasms were the detection of parenchymal CNS tumor lesions as well as clinical parameters indicating leptomeningeal involvement (such as elevated CSF cell counts, detection of suspicious or clearly malignant cells in CSF cytology, and radiological signs of LMD). Finally, patients were assessed according to the current EANO–ESMO classification guidelines for LMD.[61] In addition to the parameters from clinical routine diagnostics, tumor cell detection based on our scRNA-seq analysis was also incorporated into the final diagnostic classification, as detailed in Table S1. We aimed to cover a comprehensive spectrum of entities and therefore included patients with GB (*n* = 2), CNSL (*n* = 5), and BrM from lung

Please cite this article in press as: Nieto et al., Integrative CSF profiling identifies disease-specific immune responses in leptomeningeal disease, Cell Reports Medicine (2026), https://doi.org/10.1016/j.xcrm.2026.102651

adenocarcinoma (*n* = 2), breast cancer (*n* = 2) and melanoma (*n* = 1). Four patients served as a non-cancer CNS inflammatory control condition suffering from viral meningitis (*n* = 1), cerebral abscess with bacterial meningitis and ventriculitis (Eikanella spp. bacteria) or the CNS autoimmune disease neurosarcoidosis (*n* = 2). The median age at the time of CSF sampling was 59 years (range 33–73), with six of 16 patients being female (38%). Serial CSF samples at different time points were obtained from four patients of this cohort: patient P10 with CNS-DLBCL, patient P12 with breast cancer BrM and LMD and patient P07 with cerebral abscess. Additionally, PBMCs corresponding to the CSF samples were obtained from blood samples of patients P06 (CNS-DLBCL), P07 (cerebral abscess), P10 (CNS-DLBCL) and P12 (breast cancer BrM and LMD) with two timepoints available for patient P07 and patient P10 for scRNA-seq. Further, FFPE tissue for spatial transcriptomics was available for six patients of our cohort (patients P01 and P10 with CNS-DLBCL, patient P02 with GB, patient P07 with cerebral abscess, patient P09 with melanoma BrM and LMD, and patient P12 with breast cancer BrM and LMD).

All patients were diagnosed and treated at the University Hospital Frankfurt. Routine pathological or neuropathological workup of tissue was performed at the Departments of Pathology and/or Neuropathology (Edinger Institute). Demographic and other clinical data (such as routine CSF parameters: protein and lactate (assessed in the Department of Neurology), cytology (assessed by cytomorphology and/or immunocytochemistry and/or flow cytometry in the Departments of Neurology, Neuropathology, Pathology and Hematology as well as detailed information on disease course, treatment and sampling timepoints) were extracted from patients' records, pseudonymized, and entered into password-protected databases.

Immunohistochemistry (IHC)

Formalin-fixed, paraffin-embedded tumor tissue samples of patients analyzed by spatial transcriptomics were also analyzed with immunohistochemistry (IHC). Tissue samples were sectioned at 4 μm thickness using a microtome (Leica SM 2000R, Germany) and mounted on Superfrost Plus slides (Thermo Scientific, Germany). Immunohistochemical stainings were performed on a LEICA BOND-III automated stainer (Leica, Wetzlar, Germany) following established protocols. The following primary antibodies were used: anti-CD3 (Dako, A0452; 1:500), anti-CD8 (Dako, clone C8/144B; 1:100), anti-CD20 (Dako, clone L26; 1:500), anti-CD45/LCA (Dako, clones 2B11+PD7/26; 1:200), anti-CD68 (Dako, clone PG-M1; 1:200), and anti-panCK (Dako, clone MNF116; 1:1000). Slides were evaluated by a board-certified neuropathologist (KJW) using a brightfield microscope (BX51, field of view 22 mm; Olympus, Tokyo, Japan).

Collection and cryopreservation of cells from cerebrospinal fluid and peripheral blood mononuclear cells

All CSF samples were collected during routine clinical care, primarily through lumbar puncture, except for four samples collected by ventricular CSF sampling. CSF samples were immediately centrifuged at 400 g for 10 min to separate cell-free from cellular components. Supernatant was transferred to cryo-vials and shock frozen in liquid nitrogen. CSF cells were resuspended in 1mL of 90% FCS and 10% DMSO and slowly frozen −80°C using a Mr. Frosty. Whole blood was withdrawn in EDTA tubes and peripheral blood mononuclear cells (PBMCs) isolated using Lymphoprep (Serumwerk Bernburg) according to the manufacturer's protocol. Cells were counted by automatic cell counting using a Countess 3 FL (Invitrogen). Cells were resuspended in 90% FCS and 10% DMSO. 1mL of cell suspension with 5 million cells per mL was transferred to a cryo vial and slowly frozen at −80°C in a Mr. Frosty. For storage, all samples were transferred into liquid nitrogen.

Single cell RNA-sequencing

Cryopreserved CSF samples were thawed in a 37°C water bath and transferred to a 15 mL Falcon tube containing 10 mL of pre-warmed, pre-filtered RPMI medium supplemented with 10% FBS (Thermo Fisher Scientific). The samples were centrifuged at 400 × g for 10 min at room temperature, and the supernatant was removed, leaving behind a small volume of approximately 100 μL. One milliliter of pre-chilled RPMI medium was added to resuspend the pellets, and the cell content was estimated using the LUNA-FL counter (LogosBiosystems) after staining with Acridine Orange/Propidium Iodide. Up to 5 mL of cold RPMI medium was then added to wash the cells, followed by centrifugation at 400 × g for 10 min at 4°C. Based on cell concentration and assuming ∼30–40% cell loss during centrifugation, the samples were resuspended in an appropriate volume of cold RPMI medium to achieve a concentration of approximately 1000 cells/μL. The LUNA-FL counter was used again to verify the final cell concentration and viability of the samples.

Samples were loaded onto the Chromium X instrument (10X Genomics) and encapsulated for a target cell recovery of between 1,000 and 10,000 cells, using the standard throughput Chromium Next GEM Single Cell 5′ Reagent Kit v2 (10X Genomics, PN-1000263). Libraries were prepared following the manufacturer's instructions (protocol CG000331). Briefly, after GEM-RT cleanup, cDNA was amplified over 13 cycles, purified, and quantified on an Agilent Bioanalyzer High Sensitivity chip (Agilent Technologies). To construct the gene expression (GEX) library, 10 to 50 ng of cDNA were fragmented, end-repaired, A-tailed, and sample-indexed using the Chromium Single Cell 5′ Library Construction Kit (10X Genomics, PN-1000190) and the Dual Index Kit TT Set A (10X Genomics, PN-1000215). Human T and B cell receptor sequences were enriched from the amplified full-length cDNA using the Chromium Single Cell Human TCR/BCR Amplification Kit (PN-1000252/1000253). Fragmentation, end-repair, A-tailing, and library indexing of the enriched cDNA were performed using the aforementioned kits. Finally, the size distribution and concentration of the 5′ GEX and TCR/BCR libraries were verified on an Agilent Bioanalyzer High Sensitivity chip. Sequencing was performed on a

Please cite this article in press as: Nieto et al., Integrative CSF profiling identifies disease-specific immune responses in leptomeningeal disease, Cell Reports Medicine (2026), https://doi.org/10.1016/j.xcrm.2026.102651

NovaSeq 6000 system (Illumina), aiming for approximately 40,000 and 10,000 read pairs per cell for the GEX and TCR/BCR libraries, respectively. The sequencing conditions were 28 bp (Read 1) + 10 bp (i7 index) + 10 bp (i5 index) + 90 bp (Read 2).

Nanopore-sequencing of cell-free DNA from cerebrospinal fluid

The cfDNA was extracted from the cell free CSF fraction of the samples of 13 patients (Table S1) using the QIAmp MinElute ccfDNA Mini Kit (Qiagen) according to the manufacturer's protocols. Quantification of cfDNA was performed with a Qubit Fluorometer (Invitrogen) and using an Agilent tape station device (Agilent Technologies). Sequencing libraries were prepared using the Ligation Sequencing kit (Oxford Nanopore) with 2.7–43.3 ng input depending on sample yield. Nanopore whole-genome sequencing with ∼9.58M (SD: 6.99M) read-pairs per sample was performed using the MinION instrument (Oxford Nanopore). Sequence data were mapped to the human reference genome (hg19) within the NanoDx pipeline. Copy number profiles as well as the estimation of circulating tumor DNA fractions from CSF cfDNA were assessed by use of the NanoDx pipeline.[62,63]

Xenium In Situ analyzer

The human Spatial Transcriptomics brain data was generated on the Xenium *In Situ* platform using the pre-designed Xenium Human Immuno-Oncology panel targeting 380 genes (chemistry version 1, cat #: 1000654). Archived human brain tissues were processed according to the manufacturer's instructions (CG000578 – Rev C) after assessing sample quality by H&E and DAPI staining in adjacent tissue sections from the same blocks. 6 formalin-fixed paraffin-embedded brain sections (5 microns thick) were mounted onto two Xenium slides, incubated at 42°C for 3h and dried overnight at room temperature in a desiccator. Xenium slides were processed and analyzed 4 days after sectioning. Sections were deparaffinized and de-crosslinked (CG000580 – Rev C), and then hybridized with the pre-designed probes at 50°C overnight (∼20 h), followed by post-hybridization washes, ligation, amplification, multimodal cell segmentation staining and autofluorescence-quenching as described in user guide CG000749 – Rev A. Xenium slides were loaded on the Xenium Analyzer instrument for imaging and analysis under software version 1.3.3.0, following the Imaging user guide CG000584 – Rev E.

QUANTIFICATION AND STATISTICAL ANALYSIS (STAR METHODS)

scRNA-seq data pre-processing and quality control

To profile the cellular transcriptome, we processed the sequencing reads with 10X Genomics Inc.'s software CellRanger (version 7.0.0) and mapped them against the human reference transcriptome, GRCh38 (Genome Reference Consortium Human Build 38 Organism, version 2020-A). For the TCR libraries, the corresponding VDJ human reference was also used (version 5.0.0).

For all CSF and PBMCs scRNA-seq datasets, we performed quality control (QC) on the raw dataset count matrices by taking into account the main cell metrics: number of genes, library size/number of UMIs (unique molecular identifiers) and percentage of mitochondrial RNA content per cell. Metrics distributions were visualized across libraries and, consequently, we removed low quality observations using permissive thresholds. We applied the following filters in order to select only good quality cells from downstream analysis.

- Library size between 800 and 25000 UMIs
- Number of genes between 350 and 6000
- Mitochondrial content lower than 20%

For one of the CSF batches, where the numbers of cells loaded and recovered were lower than the others, we applied more permissive filters by lowering the library size lower threshold to 500, minimum number of genes to 200 and allowed up to 25% of mitochondrial content.

We used Scrublet as the doublet-detection algorithm, applying the default 10x Genomics parameter settings with a threshold of 0.06 on each sample separately. This threshold is not expected to substantially influence downstream results, and we did not remove cells solely on the basis of their Scrublet score at this stage. Instead, doublet calls were incorporated into downstream quality-control steps.

During clustering, we identified and removed clusters that exhibited features consistent with low-quality or artifactual populations, including: (i) elevated doublet scores, (ii) higher mitochondrial read percentages compared with other clusters, and/or (iii) co-expression of markers from distinct, incompatible lineages. Clusters meeting one or more of these criteria were annotated as potential doublets or low-quality clusters and excluded from further analysis.

Healthy cohort

We downloaded raw data (fastq files) from Piehl, Natalie et al. Cell (2022), from GEO (GSE200164) and processed them following the same pipeline as the rest of the CSF samples.

Normalization and clustering

Each scRNA-seq sample data (CSF from healthy and diseases and blood samples) was analyzed independently in order to do a preliminary cell annotation which would allow us to evaluate batch correction performance in later steps. For this we used functions from

Please cite this article in press as: Nieto et al., Integrative CSF profiling identifies disease-specific immune responses in leptomeningeal disease, Cell Reports Medicine (2026), https://doi.org/10.1016/j.xcrm.2026.102651

the Seurat package (version 4.4.0). Normalization by library size is applied to account for differences in sequencing depth across cells. Values are then scaled by a fixed factor of 10 ˆ4 and log transformed as standard single cell best practice. Following normalization, highly variable genes (HVGs) are identified to capture cell-to-cell transcriptomic variation, a critical step in defining cellular heterogeneity. We selected the top 3000 HVGs per sample. After HVG identification, the data are scaled to standardize expression across genes. This centers the data by subtracting the mean expression level and divides by the standard deviation, resulting in a Z score for each gene within each cell. Standardization is essential for ensuring that differences in expression magnitudes do not disproportionately influence downstream analyses. We ran principal component analysis (PCA) and then selected the top principal components (PCs) based on explained variance and the elbow method, to capture the most biologically relevant patterns. Subsequently, neighbor identification and clustering was applied to group cells into transcriptionally similar clusters, representing distinct cell populations. Several clustering resolutions were explored. Furthermore, Uniform Manifold Approximation and Projection (UMAP) was applied to further reduce the data's dimensionality and visualize complex transcriptional landscapes in two dimensions. This low-dimensional visualization facilitates exploration of cellular heterogeneity. We used the top 20 PCs for neighbor identification, clustering and UMAP.

General annotation

General annotation of the major cell populations was performed looking at the per-cluster expression of canonical genes: *PTPRC/CD45* (immune cells), *CD79A, CD19* (B cells), *MZB1, IGHA1, IGHG1* (Plasma cells), *CD14, CD68* (Macrophages), *S100A8, LYZ, VCAN* (Monocytes), *CD1C, CLEC9A, IL3R* (Dendritic cells), *CD3E, CD4* (CD4 T cells), *CD3E, CD8A, CD8B* (CD8 T cells), *NCAM1, NKG7, GNLY* (NK cells).

This per-sample preliminary annotation allowed us to then validate the integration downstream.

Integration and in-depth annotation

We then batch-corrected the pre-processed CSF or blood samples with the python package scVI (version 1.0.4). We integrated all disease CSF samples together, but also only the CSF myeloid cells and the CSF T cells independently, as well as all blood samples and healthy CSF samples to correct for technical artifacts and batch effects. We decided to not integrate healthy and disease CSF samples together, as the disease state and batch of origin were confounded and integration would not allow us to correctly eliminate spurious effects and accurately compare samples. For scVI integration, we adjusted parameters (number of nodes per hidden layer, dimensionality of the latent space and number of hidden layers used for encoder and decoder neural networks) for each dataset. Neighbor identification and clustering using the python package scanpy (version 1.9.6), accompanied integration. We followed a top-down approach, where we first integrated and clustered all cells to annotate the major cell populations and then re-integrated and clustered each of the interesting major cell populations alone to find subpopulations. Clustering resolution was adjusted for each dataset and, in some cases, clusters were split or merged after looking at the expression profiles. In some cases, bad quality or doublet clusters emerged and were removed from downstream analysis. UMAP was applied after integration strictly for visualization, providing a two-dimensional representation, while not contributing to any downstream analyses.

In depth characterization of T and myeloid populations was carried out by immunology experts by looking at the differentially expressed genes in each cluster and comparing it to populations described in the literature.

Tumor cell identification in CSF scRNA-seq

To identify tumor cells in scRNA-seq data, we used different approaches depending on the type of brain tumor. For GB BrM CSF samples, tumor cell signatures and relevant markers were quantified in CD45-negative cells. If some expression of the corresponding signature or markers was detected, we considered a sample positive for the presence of tumor cells.

In CNSL samples, we determined the kappa-to-lambda immunoglobulin light chain ratio on B cells, as a monoclonal light chain shift is indicative of malignancy in lymphomas. To differentiate malignant B cells from non-malignant B cells, we leveraged the fact that malignant B cells express only a single type of immunoglobulin light chain, either kappa (κ) or lambda (λ). We annotated each B cell as κ or λ based on the expression levels of the genes IGKC (which encodes a constant region of the κ chain) and IGLC1, IGLC2, IGLC3, IGLC4, IGLC5 and IGLC6 (λ chain). Unfortunately, dropout events led to varying numbers of unknown B cells in each sample. Following a similar approach to the one used by Zhao Y. et al. 2022, we calculated the κ/λ B cell ratio for each sample. If either type represented more than 50% of the B cells of a sample, we considered it positive for malignant cells. However, although the shift might have been present in most CNSL samples, unknown immunoglobulin light chains prevented us from confidently discerning the presence of malignant cells in all samples.

For inconclusive cases, additionally, we assessed genomic instability by detecting copy number variations (CNVs) using inferCNV (inferCNV of the Trinity CTAT Project. https://github.com/broadinstitute/inferCNV) version 1.3.3 in CD45-negative cells from BrM samples, as well as in B cells from CNSL samples. We configured inferCNV to analyze cells individually (analysis_mode = "cells"), using a cutoff value of 0.1, which is optimized for 10x Genomics data, as described by the package authors. CNV detection was performed in a denoised mode to minimize noise in gene expression data while enabling Hidden Markov Model (HMM)-based CNV inference. The HMM analysis was set to output consensus-based results across cells (HMM_report_by = "consensus"), employing the "i3" model, which is recommended for distinguishing between three CNV states (insertion, deletion and neutral/none). This approach allowed us to infer CNV profiles across cell populations, aiding in the identification of chromosomal regions with possible copy

Please cite this article in press as: Nieto et al., Integrative CSF profiling identifies disease-specific immune responses in leptomeningeal disease, Cell Reports Medicine (2026), https://doi.org/10.1016/j.xcrm.2026.102651

number gains or losses. Reference cell types for BrM samples were all immune cells while we only used myeloid and T cells in the case of CNSL samples.

TCR data analysis

We defined TCR clonotypes as T cells with an exact overlap in beta-chain receptor amino acid sequence. We used scRepertoire (version 1.12.0) to combine gene expression and TCR information from the same cells. Only TCR sequences associated with cells annotated as T cells by RNAseq were kept for downstream analysis.

Signature scoring and pseudobulk analysis

Signature scoring was performed in two different ways. At the single cell level, signatures were computed by cell, using the UCell R package (version 2.6.2). At the patient or disease level, we first aggregated the counts for a specific cell type or across all the cells for each patient or disease, by computing a "pseudobulk" using the presto R package (version 1.0.0) which were then normalized. We then scored signatures using decoupleR (version 2.8.0), on the pseudobulks by applying either a multivariate linear model (MLM) or a weighted sum (WSUM) method. For the Xenium data, signature scores per cell were computed using AUCell and divided by the cell area. Then score values within the range between the 1st and 99th percentiles of each signature were selected and scaled prior to visualization. We used validated gene signatures from prior literature to build our own signatures. all the signatures are in a table used in each case and can be found in Table S4.

Compositional analysis

To estimate changes in cell population proportions across various diseases, we used the scCODA Python package, a Bayesian modeling tool designed to account for the compositional nature of single-cell data and reduce the likelihood of false discoveries. It enables us to infer shifts between conditions while incorporating additional covariates. It detects differences between a reference cell type, assumed to remain constant across conditions, and the other cell types. To conduct our analysis in an unsupervised manner, we allowed scCODA to automatically select this reference. scCODA takes as input the number of cells of each cell type in each patient and outputs the list of proportion changes for cell types, along with corresponding corrected *p*-values (adjusted through the False Discovery Rate procedure, FDR).

Gene co-expression network analysis

We performed weighted gene co-expression network analysis within the myeloid cell population of our scRNA-seq dataset using the R package hdWGCNA (version 0.4.0). Genes expressed in fewer than 5% of cells were excluded, yielding 9,982 genes. We next used the hdWGCNA function *MetacellsByGroups* to construct de-noised metacell gene expression profiles for each patient using the level 2 cell annotations. A soft-power threshold on the gene-gene co-expression network was optimized using the hdWGCNA function *TestSoftPower*. Using the hdWGCNA function *ConstructNetwork*, we computed a topological overlap matrix (TOM) to represent the gene co-expression network and grouped genes into 14 modules with the Dynamic Tree Cut algorithm. One of these modules was removed from downstream analysis, as it was the smallest of them and contained only 56 genes. Specific parameters for these functions can be found in the GitHub repository associated with this manuscript. The steps of this co-expression network analysis were repeated for the myeloid cell population in the healthy CSF scRNA-seq dataset to facilitate comparisons at the network level. We performed a pairwise gene set overlap analysis between modules identified in the disease CSF dataset versus the healthy CSF dataset using the R package GeneOverlap[64] (version 1.38.0), which performs a Fisher's exact test to quantify statistical significance and effect size of the overlap compared to a background set of genes.

Cell communication analysis

For cell-cell communication analysis, we used the CellChat R package (version 2.1.2), which infers intercellular communication networks by analyzing ligand-receptor gene pairs in scRNA-seq data. Starting with a normalized, clustered single-cell dataset, we first created a CellChat object for each interesting sample, patient or disease group, to store the expression data and metadata information (general cell types). We then subset the data to include only expressed genes, to retain ligand-receptor pairs with significant expression in each cluster, following the recommended pipeline described by the package authors. We then mapped gene expression data onto the known CellChat database of human ligand-receptor interactions. We identified cell populations with significant changes in sending or receiving interacting signals and visualized the inferred communication strengths and directions.

Xenium data analysis

Raw Xenium data were QC-ed to remove only empty cells (cells containing no transcripts). In order to annotate the cells to a general level, we combined information from the immuno-oncology panel annotation and canonical marker expression and aggregated the transcript counts in each cell, by cell type. Cells were annotated as the cell type they contained more transcripts of, therefore some cells were labeled as unknown. We validated this annotation method by computing cell-type signature scores with the R package AUCell (version 1.24.0), using the same gene sets for each cell type.

Please cite this article in press as: Nieto et al., Integrative CSF profiling identifies disease-specific immune responses in leptomeningeal disease, Cell Reports Medicine (2026), https://doi.org/10.1016/j.xcrm.2026.102651

Statistical analysis and data visualization

All analyses presented in this manuscript were carried out using the programming languages R, versions 4.2.3 (2023-03-15) and 4.3.3 (2024-02-29), and Python version 3.8.5. More details about specific packages and functions used can be found in the Github repository associated with this publication. Detailed information on the statistical analyses and significant levels are indicated in the figure legends and text when necessary. Illustrations were created with Biorender (https://www.biorender.com/) and figures were put together using Inkscape (https://inkscape.app/).

Boxplots

To summarize and visualize the distribution of the data, we used *geom_boxplot()* from the ggplot2 package in R (version 3.5.1). This function generates a boxplot, which provides an overview of key summary statistics, including the median, interquartile range (IQR), and potential outliers. The boxplot allows for an efficient comparison of distributions across different groups within the data. The central box represents the interquartile range (IQR) of the data, which spans from the 25th percentile (the first quartile, Q1) to the 75th percentile (the third quartile, Q3). Within this box, a horizontal line marks the median (50th percentile) of the data, providing a measure of central tendency. The "whiskers" extend from the box up to a maximum of 1.5 times the IQR above Q3 and below Q1, covering most of the non-outlier data points. Points beyond the whiskers are considered potential outliers and are plotted individually as dots.